This article has been accepted for publication in a future issue of this journal, but has not been fully edited. Content may change prior to final publication. Citation information: DOI 10.1109/TEC.2020.2965017, IEEE Transactions on Energy Conversion

Effect of Reactive Power Characteristic of Offshore Wind Power Plant on Low-Frequency Stability

Weihua Zhou, *Student Member, IEEE*, Yanbo Wang, *Senior Member, IEEE*, Raymundo E. Torres-Olguin, and Zhe Chen, *Fellow, IEEE*

***Abstract*—Oscillation phenomena of offshore wind power plant (OWPP) in a wide frequency range can be caused due to impedance interactions between grid-connected inverters (GCIs) and transmission cables. In this paper, impedance model of GCI with outer power control loop, inner current control loop and phase-locked loop is first established in dq reference frame. The correctness is validated by frequency scanning method. Then, the effects of active and reactive power/current references on dq impedance characteristics of GCI with/without consideration of power control loop are investigated using complex space vectors and complex transfer functions. Furthermore, RLC circuit model of transmission cable considering frequency-dependent characteristics is also established for dq-domain IBSC. On the basis of them, it's found that low-frequency oscillation phenomena of OWPP under power control mode may occur if active power reference exceeds a certain threshold value, which can be mitigated by injecting a certain amount of negative reactive power. Impacts of PLL parameters, length of transmission cable and number of paralleled GCIs on required negative reactive power for low-frequency stabilization are further investigated. Both Matlab/Simulink-based simulation and OPAL-RT-based real-time verification are implemented in an OWPP with four permanent magnet synchronous generators to validate the correctness of the reactive power characteristic analysis results and the feasibility of mitigating low-frequency oscillation phenomena by negative reactive power injection.**

***Index Terms*—Frequency scanning, grid-connected inverter, low-frequency stability, offshore wind power plant, reactive power, transmission cable.**

I. Introduction

OFFSHORE wind power plants (OWPPs) are increasingly explored in recent years, which are commonly connected into utility grid by transmission cables [1]. Grid-connected inverter (GCI), as an important power electronic interface, is frequently used to deliver electricity to utility grid [2]. Recently, oscillation phenomena of OWPPs in a wide frequency range due to dynamic interactions between control loops of GCIs and time-varying grid impedance have been frequently reported [3]–[8].

Control loops of the GCI mainly include outer power control loop, inner current control loop and phase-locked loop (PLL), which are used to perform power regulation, current regulation and grid synchronization, respectively [7]. Impedance-based stability criterion (IBSC) for three-phase GCI has been proposed to investigate these oscillation phenomena, where impacts of the control loops on terminal impedance have been investigated by various impedance models [3]–[7], [9]–[14]. The mechanism of high-frequency instability phenomena induced by the interaction between inner current control loop and transmission cable is investigated in [6], [10], [11]. The analysis results indicate that the impedance formula of a GCI with only consideration of inner current control loop does not consist of active power reference. Therefore, the high-frequency stability dominated by the inner current control loop is not affected by active power level [11], [15]. Output impedance of the GCI further considering PLL can be represented as a two-dimensional matrix, which is diagonal dominant if the GCI is operated under high power factor condition [7]. However, the high power factor condition is not commonly satisfied in practical application, since the GCIs are sometimes controlled to inject reactive power [12], [16], [17]. The recent study in [7], [18] shows that magnitude of cross-coupling term of the two-dimensional impedance matrix can be increased once reactive current reference is increased, whereas the quadrature-axis impedance which reflects the negative resistor feature of PLL in low-frequency range is not affected. In addition, stability analysis of the GCI considering outer power control loop is implemented in [19], where eigenvalue analysis indicates that controller parameters of the outer power control loop have an important effect on stability in low-frequency range. However, the effect of power operation point, i.e., active and reactive power references, on stability has not been studied. Impedance model of the GCI with both inner current control loop and outer power control loop is established in [13], [14], which is related with active and reactive power references. Furthermore, instability phenomena in a two-terminal VSC-HVDC system can be caused by high active power reference [13], [20]. Also, flow direction of active power of two-terminal and three-terminal VSC-HVDC systems can influence system stability [14]. However, impacts of power level and flow direction of reactive power on system stability have slightly been analyzed.

In addition to the aforementioned works about stability analysis of offshore wind generators connected to long transmission cables, extensive researches about stability analysis of solar PV generators which work under weak grid condition have been reported in [21]–[24]. The stability issues of PV inverters connected with weak grid considering effects of inner

This work was supported by the ForskEL and EUDP project "Voltage Control and Protection for a Grid towards 100% Power Electronics and Cable Network (COPE)" (Project No.: 880063).

W. Zhou, Y. Wang, and Z. Chen are with the Department of Energy Technology, Aalborg University, Aalborg 9220, Denmark (e-mail: wez@et.aau.dk; ywa@et.aau.dk; zch@et.aau.dk).

R. E. Torres-Olguin is with the SINTEF Energy Research Institute, Trondheim 7034, Norway (e-mail: raymundo.torres-olguin@sintef.no).

This article has been accepted for publication in a future issue of this journal, but has not been fully edited. Content may change prior to final publication. Citation information: DOI 10.1109/TEC.2020.2965017, IEEE Transactions on Energy Conversion

current control loop on both low-frequency and high-frequency stability are initially investigated in [21]. Furthermore, it is found in [22] that increase of grid impedance can suppress the low-frequency instability, whereas the increase of grid impedance can degrade the high-frequency stability. In [23], a probabilistic method is presented to analyze the small-signal stability of power systems with PV integration considering variation and uncertainty of solar irradiation. In [24], a nonlinear describing function method is presented to perform the accurate stability analysis of PV generators with consideration of the nonlinear and discontinuous perturbation and observation-based power control. However, only stability analysis methods of PV generators connected with weak grid are developed in [21]–[24], whereas no further stability enhancement strategies are explored. In [18], [25]–[30], dq impedance model of the GCI is reshaped to mitigate the negative effect of PLL on low-frequency stability. In [18], the stability margin under weak grid condition is improved by optimizing current controller parameters. In [25], [26], the stability margin under weak grid condition is improved by decreasing PLL bandwidth. However, system dynamic performances will be degraded, if a lower PLL bandwidth is adopted. In [27]–[30], grid voltage feed-forward control strategies are used to reshape the quadrature-axis impedance to mitigate the negative effect of PLL on low-frequency stability. However, too large or too small grid voltage feed-forward coefficient can degrade system stability, which makes it difficult to select optimal value [30]. In addition, only inner current control loop and PLL, instead of outer power control loop, are considered in [18], [21]–[30].

Similar with OWPP case, reactive power injection has been a well-developed solution of PV applications for voltage support [31], for power transfer capability improvement [32], and for power losses minimization [33]. However, few researches have been reported to reshape the quadrature-axis impedance through adjusting power operation point. Case studies in [7] show that reactive power injection affects all the four components of the dq impedance model when further considering outer power control loop. However, quantitative and general analysis of the impacts of reactive power injection on quadrature-axis impedance and corresponding system stability has not been performed yet. To the best of the authors' knowledge, there is no report about the application of the reactive power injection in either OWPP case or PV case to mitigate low-frequency instability phenomena through reshaping quadrature-axis impedance. The low-frequency stabilization approach presented in this paper may explore the inherent capability of the GCI to mitigate low-frequency instability phenomena under weak grid condition by injecting negative reactive power.

Besides the aforementioned dq impedance models of GCIs, it's also important to establish accurate circuit models of transmission cables to reproduce practical terminal impedance feature for dq-domain IBSC. Previous works about circuit modelling of transmission cable have been presented in [10], [11], [34]–[39]. The established circuit models of transmission cables in [10], [11], [34]–[36] are used for phasor-domain IBSC. In [34], the transmission cable is modelled as a Π section which consists of a series inductor and two parallel capacitors, which fails to reveal practical frequency characteristics and may perform inaccurate stability assessment. Furthermore, circuit models of transmission cables with consideration of distributed parasitic capacitance are established in [10], [11], [35], in which multiple-cascaded Π-section circuit model is used. However, per-unit-length (p.u.l.) resistance and inductance of transmission cable are still regarded as constant, which cannot reveal practical frequency-dependent characteristics and corresponding damping characteristics. To simulate practical frequency characteristics of transmission cables, extra RL branches are inserted into each Π section in parallel connection in [37]–[39]. However, the established frequency-dependent circuit models are used for state space model-based eigenvalues analysis. Whether the RLC circuit model of transmission cable considering frequency-dependent characteristics is applicable for dq-domain IBSC should further be investigated.

In this paper, dq impedance models of GCIs with only inner current control loop and PLL, and with outer power control loop, inner current control loop and PLL are first established, respectively. A frequency scanning scheme is also developed to verify the correctness of the established dq impedance models. The effects of active and reactive current/power references on dq impedance feature, especially on quadrature-axis impedance feature, are then theoretically derived using complex space vectors and complex transfer functions. On its basis, a quadrature-axis impedance reshaping method through negative reactive power injection for low-frequency stability improvement is presented. In addition, circuit model of transmission cable considering frequency-dependent characteristics of p.u.l. resistance and inductance is established for dq-domain IBSC. The correctness of the effects of active and reactive current/power references on quadrature-axis impedance feature and corresponding system stability is validated in an OWPP. In addition, the effectiveness of the proposed low-frequency stabilization method based on negative reactive power injection is verified with variation of PLL bandwidth, grid strength and number of operating inverters.

Main contributions of this paper are summarized as follows.

(1) The dq impedance models of the GCI without and with consideration of outer power control loop are reformulated using complex space vectors and complex transfer functions, which facilitates the observation of effects of different control loops on dq impedance model.

(2) The impact of reactive current/power injection on dq impedance model under current/power control mode, especially on quadrature-axis impedance, is theoretically derived, which shows that the quadrature-axis impedance without outer power control loop remains unchanged with variation of reactive power injection, whereas the quadrature-axis impedance will be affected by outer power control loop.

(3) Circuit model of transmission cable considering frequency-dependent feature is established for dq-domain IBSC, which is able to obtain an accurate impedance-based stability analysis result.

(4) A quadrature-axis impedance reshaping method through negative reactive power injection to improve low-frequency

This article has been accepted for publication in a future issue of this journal, but has not been fully edited. Content may change prior to final publication. Citation information: DOI 10.1109/TEC.2020.2965017, IEEE Transactions on Energy Conversion

stability is presented, where the amount of required reactive power under a specific weak grid condition can be obtained.

The rest of this paper is organized as follows. In Section II, system configuration of the studied OWPP is introduced, followed by impedance modelling of GCIs and transmission cables. In Section III, the effects of reactive power injection on quadrature-axis impedance feature of current-controlled and power-controlled GCIs are theoretically analyzed, based on which the quadrature-axis impedance reshaping method through negative reactive power injection is presented. The correctness of the analysis results is validated in Section IV. On its basis, in Section V, impacts of PLL parameters, grid strength and number of operating GCIs on required negative reactive power for low-frequency stabilization are analyzed and validated. Finally, conclusions are drawn in Section VI.

II. System Configuration and Impedance Modelling

In this section, system configuration of an exemplified OWPP is first depicted, followed by establishing dq impedance matrix of GCI with consideration of outer power control loop, inner current control loop and PLL. Also, circuit model of transmission cable considering frequency-dependent feature is established.

A. System Configuration

Fig. 1(a) shows the circuit configuration of an exemplified OWPP, where four permanent magnet synchronous generators (PMSGs) are connected with point of common coupling (PCC) through 575 V/ 33 kV transformers T1, T2, T3, T4 and transmission cables TC1, TC2, TC3, TC4. And the 33 kV bus is connected into 150 kV main AC grid through 33 kV/150 kV transformer T5 and transmission cable TC5.

For each PMSG, controls of generator side converter and GCI are decoupled, and dc-link voltage V_{dc} is regarded as constant [10]. Therefore, output impedances of the four PMSGs are only dependent on the four GCIs. The control structure of the GCIs is shown in Fig. 1(b), where outer power control loop, inner current control loop and PLL are marked as blue, black and red, respectively. Although many PLL structures different from each other by the phase detectors have been proposed, they share the same phase-locking principle and differ mainly in the area of phase-angle measurement [40]. Its impact on the converter output impedance is negative, which is not changed by advanced PLL, current, and power control strategies [7]. Therefore, the synchronous reference frame-PLL (SRF-PLL) which is currently the most common phase-locked method is used in this paper.

Instability phenomena may occur under weak grid condition. Specifically, the grid is regarded as weak if it has a high impedance seen from PCC, which can be depicted by the short-circuit ratio (SCR), shown as follows [32].

$$SCR = \frac{P_{SC}}{P_{OWPP\_rated}} = \frac{V_g^2/|Z_g|}{P_{OWPP\_rated}} \tag{1}$$

where P_{SC} and P_{OWPP_rated} are the short-circuited capacity of the grid at the PCC and the rated generation power of the

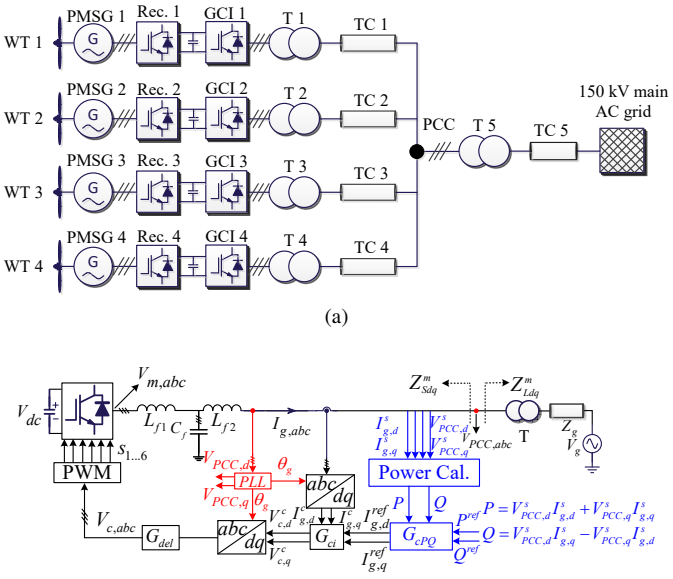

Fig. 1. Typical configuration of an HVAC-connected OWPP. (a) Four PMSGs connected with PCC via transmission cables in parallel. (b) Control structure of the four GCIs.

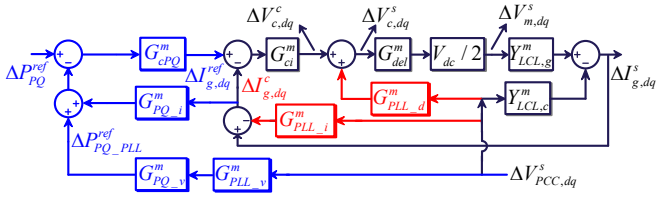

Fig. 2. Block diagram of the GCIs in Fig. 1 using transfer matrices [7].

OWPP, respectively. Generally, the grid is weak when $2 \leq SCR \leq 3$ and very weak when $SCR < 2$ [18].

B. DQ Impedance Modelling of GCI

Output impedances of L-filtered GCI without and with outer power control loop have been derived in [7]. On its basis, dq impedance models of LCL-filtered GCIs without and with power control loop can be established based on the control block diagram in Fig. 2, shown as (2) and (3) on the next page, where $Y^m_{LCL,c}$ and $Y^m_{LCL,g}$ are defined as follows.

$$\begin{aligned} Y^m_{LCL,c} &= -\Delta I^s_{g,dq}(\Delta V^s_{PCC,dq})^{-1}\Big|_{\Delta V^s_{m,dq}=0} \\ &= (((Z^m_{L_{f1}})^{-1} + (Z^m_{C_f})^{-1})^{-1} + Z^m_{L_{f2}})^{-1} \\ Y^m_{LCL,g} &= \Delta I^s_{g,dq}(\Delta V^s_{m,dq})^{-1}\Big|_{\Delta V^s_{PCC,dq}=0} \\ &= (Z^m_{L_{f2}}(I^m + ((Z^m_{L_{f2}})^{-1} + (Z^m_{C_f})^{-1})Z^m_{L_{f1}}))^{-1} \end{aligned} \tag{4}$$

where the superscript m denotes matrix. Detailed expressions of the symbols in (2) and (3) are shown in Appendix A. It can be seen that the two PLL-related transfer matrices ($G^m_{PLL\_i}$ and $G^m_{PLL\_d}$) and the three power control loop-related transfer matrices ($G^m_{PLL\_v}$, $G^m_{PQ\_i}$ and $G^m_{PQ\_v}$) are highly sensitive to

This article has been accepted for publication in a future issue of this journal, but has not been fully edited. Content may change prior to final publication. Citation information: DOI 10.1109/TEC.2020.2965017, IEEE Transactions on Energy Conversion

$$Z^m_{LCL\_no\_PCL} = \begin{bmatrix} Z^{PLL}_{dd} & Z^{PLL}_{dq} \\ Z^{PLL}_{qd} & Z^{PLL}_{qq} \end{bmatrix} = -\Delta I^s_{g,dq}(\Delta V^s_{PCC,dq})^{-1}\Big|_{\Delta I^{ref}_{g,dq}=0}$$
$$= (Y^m_{LCL,c} - \frac{1}{2}V_{dc}Y^m_{LCL,g}G^m_{del}(G^m_{ci}G^m_{PLL\_i} + G^m_{PLL\_d}))^{-1} \cdot (I^m + \frac{1}{2}V_{dc}Y^m_{LCL,g}G^m_{del}G^m_{ci}) \quad (2)$$

$$Z^m_{LCL\_with\_PCL} = \begin{bmatrix} Z^{PCL}_{dd} & Z^{PCL}_{dq} \\ Z^{PCL}_{qd} & Z^{PCL}_{qq} \end{bmatrix} = -\Delta I^s_{g,dq}(\Delta V^s_{PCC,dq})^{-1}\Big|_{\Delta P^{ref}_{PQ}=0}$$
$$= (Y^m_{LCL,c} - \frac{1}{2}V_{dc}Y^m_{LCL,g}G^m_{del}((G^m_{ci} + G^m_{ci}G^m_{cPQ}G^m_{PQ\_i})G^m_{PLL\_i} + G^m_{PLL\_d} - G^m_{ci}G^m_{cPQ}G^m_{PQ\_v}G^m_{PLL\_v}))^{-1}$$
$$\cdot (I^m + \frac{1}{2}V_{dc}Y^m_{LCL,g}G^m_{del}(G^m_{ci} + G^m_{ci}G^m_{cPQ}G^m_{PQ\_i})) \quad (3)$$

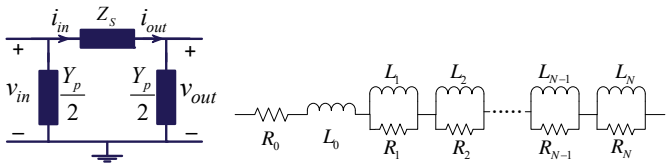

(a) (b)

Fig. 3. Circuit model of transmission cable. (a) Two-port network model. (b) RL circuit model of p.u.l. series impedance.

operating point $V^s_{PCC,dq}$, $I^s_{g,dq}$ and D^s_{dq}. The effects of the operation point on dq impedance model will be investigated in Section III.

C. Circuit Modelling of Transmission Cable with Consideration of Frequency-Dependent Characteristics

1) Practical Electrical Characteristics of Transmission Cable: Transmission cable can be modelled as a two-port network, as shown in Fig. 3(a). The parameters are given as follows [41].

$$Z_S = z(\omega)L\frac{\sinh(\gamma(\omega)L)}{\gamma(\omega)L}$$
$$Y_P = y(\omega)L\frac{\tanh(\gamma(\omega)L/2)}{\gamma(\omega)L/2} \quad (5)$$

where Z_S and Y_P are series impedance and shunt admittance; $z(\omega) = r(\omega) + j\omega l(\omega)$ and $y(\omega) = g(\omega) + j\omega c(\omega)$ the p.u.l. impedance and admittance; $\gamma(\omega) = \sqrt{(z(\omega)y(\omega)}$ propagation constant, and L the length of transmission cable; $r(\omega)$, $l(\omega)$, $g(\omega)$ and $c(\omega)$ p.u.l. resistance, inductance, conductance and capacitance, respectively. For transmission cable, $r(\omega)$ and $l(\omega)$ change as frequency varies. $g(\omega)$ can be ignored, and $c(\omega)$ is regarded as constant [41].

2) Generate Cascaded Π*-Section Circuit Model of Transmission Cable:* In the proposed circuit modelling method, $r(\omega)$, $l(\omega)$ and $c(\omega)$ are first calculated by Matlab toolbox $power\_cableparam$ based on the material and size of the transmission cable [42]. On its basis, vector fitting (VF) algorithm is then employed to fit frequency characteristics of p.u.l. series impedance $z(\omega)$. The mathematical representation can be obtained as follows [43].

$$f(s) = \sum_{n=1}^{N} B_n/(s - A_n) + D + sE \quad (6)$$

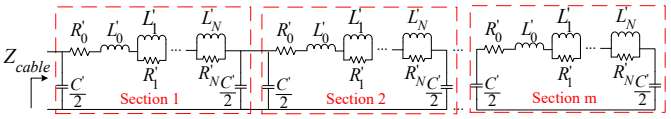

Fig. 4. Multi-segment lumped-parameter RLC circuit model of transmission cable.

where $f(s)$ is the fitted transfer function, N is the order of $f(s)$, B_n and A_n are the nth residue and pole pair. D is nonzero if the order of the numerator polynomial is not lower than the order of denominator polynomial. Nonzero E indicates the transfer function is improper [43].

(6) is then represented by an RL network, as shown in Fig. 3(b), where parameters of the RL circuit are calculated as follows.

$$R_0 = D - \sum_{i=1}^{n} B_n/A_n \quad L_0 = E$$
$$R_k = B_k/A_k \quad L_k = -R_k/A_k \quad (k = 1, 2...N) \quad (7)$$

Finally, cascaded Π-section circuit model of the transmission cable is established, as shown in Fig. 4, where the parameters of each Π section are calculated as follows.

$$R'_0 = R_0L/m \quad L'_0 = L_0L/m \quad R'_k = R_kL/m$$
$$L'_k = L_kL/m \quad C' = cL/m \quad (k = 1, 2...N) \quad (8)$$

where L is cable length, m number of Π sections, c p.u.l. capacitance. Basically, m increases as L increases. In addition, N increases as frequency range of interest widens.

Note that the impedance models of GCIs (2) and (3) are established in dq-domain, whereas the impedance model of transmission cable in Fig. 4 is established in phasor-domain. The impedance models of GCIs and transmission cable should also be represented in phasor-domain and dq-domain, respectively, to investigate the impedance interaction. The phasor-domain impedance model of the GCI can be obtained as follows [44].

$$Z^m_{inv\_pn} = \begin{bmatrix} Z_{inv\_pp} & Z_{inv\_pn} \\ Z_{inv\_np} & Z_{inv\_nn} \end{bmatrix} = A^m_Z Z^m_{inv\_dq}(A^m_Z)^{-1} \quad (9)$$

where $Z^m_{inv\_dq}$ and $Z^m_{inv\_pn}$ are dq-domain and modified sequence-domain impedance models of the GCI, respectively. $A^m_Z = \frac{1}{\sqrt{2}}[1, j; 1, -j]$, $Z_{inv\_pp} = Z_{inv}(s + j\omega_1)$, $Z_{inv\_nn} = Z_{inv}(s - j\omega_1)$. Z_{inv} is the phasor-domain impedance model.

This article has been accepted for publication in a future issue of this journal, but has not been fully edited. Content may change prior to final publication. Citation information: DOI 10.1109/TEC.2020.2965017, IEEE Transactions on Energy Conversion

On the other hand, the dq-domain impedance model of the transmission cable can be obtained as follows.

$$Z^m_{TC\_dq} = (A^m_Z)^{-1} Z^m_{TC\_pn} A^m_Z = (A^m_Z)^{-1} \begin{bmatrix} Z_{TC\_pp} & Z_{TC\_pn} \\ Z_{TC\_np} & Z_{TC\_nn} \end{bmatrix} A^m_Z \quad (10)$$

where $Z^m_{TC\_dq}$ and $Z^m_{TC\_pn}$ are dq-domain and modified sequence-domain impedance models of the transmission cable, respectively. $Z_{TC\_pn} = Z_{TC\_np} = 0$, $Z_{TC\_pp} = Z_{cable}(s + j\omega_1)$, $Z_{TC\_nn} = Z_{cable}(s - j\omega_1)$. Z_{cable} is the phasor-domain impedance model in Fig. 4.

3) Comparison of Different Circuit Models of Transmission Cable for Stability Analysis: Circuit and controller parameters of the GCIs are shown in Table I, where the bandwidths of inner current control loop, outer power control loop and PLL are 278 Hz, 13 Hz and 111 Hz, respectively. In addition, the material and physical parameters of the transmission cables can be found in [42]. Based on the material and physical parameters, the OPAL-RT ARTEMiS-SSN library is able to generate the WideBand Line model which can accurately reproduce terminal impedance characteristics [45]. Therefore, the WideBand Line model will be regarded as a benchmark to assess the accuracy of the fitted RLC circuit models. The Bode diagram of the WideBand Line model for a 11 km transmission line, i.e., SCR= 3.27, is plotted as $Z_{wideband}$ in Fig. 5(a).

Furthermore, Matlab toolbox *power_cableparam* is used to calculate $r(\omega)$ and $l(\omega)$. On its basis, $z(\omega)$ is fitted as (6) using VF algorithm, and frequency-dependent RLC circuit models in form of Fig. 4 is established based on (7) and (8). Specifically, Bode diagrams of the frequency-dependent RLC circuit models with different number of Π sections (1, 5, 10 and 20) $Z_{FD\_1\_Pi}$, $Z_{FD\_5\_Pi}$, $Z_{FD\_10\_Pi}$, $Z_{FD\_20\_Pi}$ for the 11 km transmission cable are plotted in Fig. 5(a). It can be seen that fitting accuracy becomes higher as the number of cascaded Π sections increases. On the other hand, Bode diagram of terminal impedance of RLC circuit model which consists of 20 Π sections without consideration of frequency-dependent characteristics $Z_{non\_FD\_cable}$ is plotted in Fig. 5(b). It can be seen that the non-frequency-dependent RLC circuit model cannot reveal practical damping characteristics, especially in high-frequency range.

TABLE I
CIRCUIT AND CONTROLLER PARAMETERS OF THE GCIS

Parameter	Value
DC-link voltage V_{dc}	1150 V
Grid fundamental frequency f_1	50 Hz
Inverter side filter inductance L_{f1}	263 μH
Grid side filter inductance L_{f2}	200 μH
Filter capacitance C_f	40 μF
Switching frequency f_{swit}	2.5 kHz
Sampling frequency f_{samp}	2.5 kHz
Grid Vrms (phase-to-phase) V_g	33 kV
Proportional gain of power controller k_{pPQ}	2.7454e-04
Integral gain of power controller k_{iPQ}	0.165
Proportional gain of current controller k_{pi}	1.4054e-3
Integral gain of current controller k_{ii}	0.2455
Proportional gain of PLL k_{ppll}	20
Integral gain of PLL k_{ipll}	200

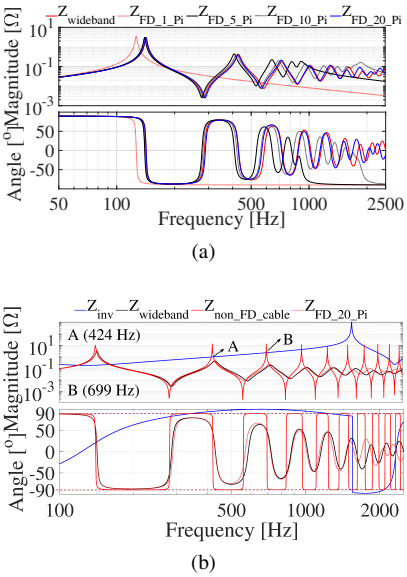

Fig. 5. Comparison of different circuit models of transmission cable for stability analysis. (a) Bode diagrams of output impedances of WideBand Line model and RLC circuit models for 11 km transmission cable. (b) Bode diagrams of output impedances of GCI 1 and 11 km transmission cable using different circuit models.

Three-phase voltages and currents when GCI 1 is connected with the 11 km transmission cable using the non-frequency-dependent circuit model with 20 Π sections, WideBand Line model and frequency-dependent circuit model with 20 Π sections are shown in Figs. 6(a), 7(a) and 7(b), respectively. It can be seen that the system is unstable in Fig. 6(a) and stable in Figs. 7(a),(b). In addition, frequency spectrum of Fig. 6(a) is shown in Fig. 6(b), where oscillation phenomena occur at 427 Hz and 714 Hz. To reveal the high-frequency oscillation phenomena, phasor-domain impedance model of GCI 1 Z_{inv} is calculated from (2) using matrix transformation (9), and Bode diagram of Z_{inv} is plotted in Fig. 5(b). It can be seen that magnitudes of Z_{inv} and $Z_{non\_FD\_cable}$ interact at both 424 Hz and 699 Hz, where phase angle differences are higher than 180^o. It indicates that the system is unstable at the two frequency points. In addition, magnitudes of $Z_{wideband}$ and $Z_{FD\_20\_Pi}$ do not interact with Z_{inv} in non-passive region of GCI 1, which indicates that the system is stable. The analysis results agree with the simulation results in Figs. 6 and 7. Since low-frequency stability is focused in this paper, and the low-frequency impedance characteristic of transmission cable can be reproduced by one Π section, the proposed one-Π-section-based frequency-dependent RLC circuit modelling method of transmission cable will be used in Sections IV and V for the dq impedance-based stability analysis of the OWPP shown in Fig. 1(a).

III. IMPACTS OF ACTIVE AND REACTIVE POWER ON DQ IMPEDANCE FEATURE OF THE GCI

In this section, impacts of active and reactive current/power references on low-frequency dq impedance characteristics of the GCI are first theoretically derived using complex space vectors and complex transfer functions. On its basis, a

This article has been accepted for publication in a future issue of this journal, but has not been fully edited. Content may change prior to final publication. Citation information: DOI 10.1109/TEC.2020.2965017, IEEE Transactions on Energy Conversion

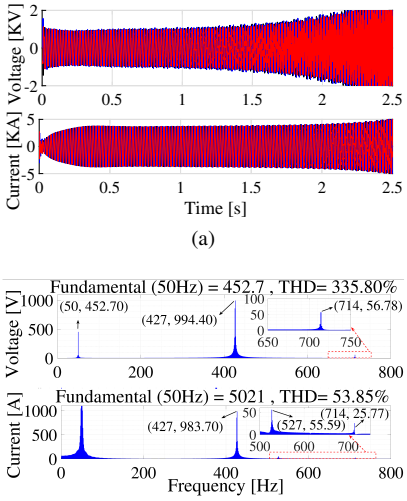

Fig. 6. Simulation results using non-frequency dependent circuit model with 20 Π sections. (a) Time-domain simulation results. (b) Frequency spectrum of three-phase voltages and currents.

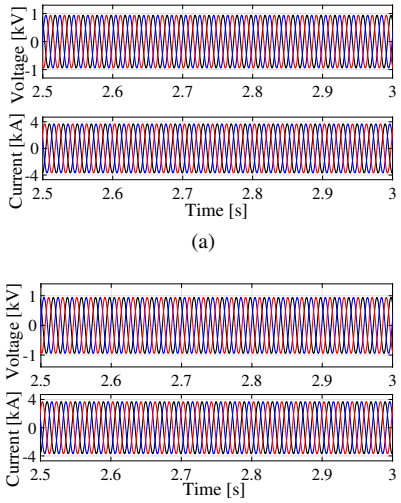

Fig. 7. Time-domain simulation results using WideBand Line model and frequency-dependent circuit model with 20 Π sections. (a) Simulation results using the WideBand Line model. (b) Simulation results using frequency-dependent circuit model with 20 Π sections.

quadrature-axis impedance reshaping method through reactive power injection is presented.

A. Theoretical Derivation of Impacts of Active and Reactive Current/Power References on DQ Impedance Characteristics

The dq impedance models in (2) and (3) will be reformulated using complex space vectors and complex transfer functions to clearly observe the effects of different control loops on dq impedance characteristics. The complex transfer function representations of the transfer matrices in (2) and (3) are listed in Appendix A, based on which the complex transfer functions-based control block diagram of the GCIs is derived in Fig. 8.

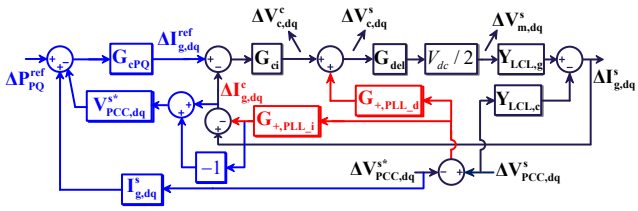

Fig. 8. Block diagram of the GCIs in Fig. 1 using complex space vectors and complex transfer functions.

1) Without Outer Power Control Loop: The closed-loop response of $\mathbf{\Delta I^s_{g,dq}}$ can be derived from Fig. 8, shown as follows.

$$-\mathbf{\Delta I^s_{g,dq}}\big|_{\mathbf{\Delta I^{ref}_{g,dq}}=0} = \mathbf{Y^{CCL}_{cl,dq}\Delta V^s_{PCC,dq}} - \mathbf{Y^{PLL}_{cl,dq}\Delta V^s_{PCC,dq}} + \mathbf{Y^{PLL}_{cl,dq}\Delta V^{s*}_{PCC,dq}} \tag{11}$$

where $\mathbf{Y^{CCL}_{cl,dq}}$ and $\mathbf{Y^{PLL}_{cl,dq}}$ are the complex transfer function representations of current control loop-related and PLL-related output admittance, respectively, shown as follows.

$$\begin{aligned}\mathbf{Y^{CCL}_{cl,dq}} &= \mathbf{Y_{LCL,c}}/(1+\mathbf{T_{cl,dq}})\\ \mathbf{Y^{PLL}_{cl,dq}} &= (\frac{\mathbf{G_{+,PLL\_d}}}{\mathbf{G_{ci}}} + \mathbf{G_{+,PLL\_i}})\mathbf{G^{CCL}_{cl,dq}}\end{aligned} \tag{12}$$

where $\mathbf{G^{CCL}_{cl,dq}} = \mathbf{T_{cl,dq}}/(1+\mathbf{T_{cl,dq}})$ and $\mathbf{T_{cl,dq}} = \frac{1}{2}V_{dc}\mathbf{Y_{LCL,g}G_{del}G_{ci}}$ are the closed-loop and open-loop gains of the current control loop, respectively.

When $\mathbf{\Delta I^{ref}_{g,dq}} = 0$, the following equation can be obtained based on (11).

$$-\begin{bmatrix}\mathbf{\Delta I^s_{g,dq}}\\ \mathbf{\Delta I^{s*}_{g,dq}}\end{bmatrix} = \begin{bmatrix}\mathbf{Y^{CCL}_{cl,dq}} - \mathbf{Y^{PLL}_{cl,dq}} & \mathbf{Y^{PLL}_{cl,dq}}\\ \mathbf{Y^{PLL*}_{cl,dq}} & \mathbf{Y^{CCL*}_{cl,dq}} - \mathbf{Y^{PLL*}_{cl,dq}}\end{bmatrix}\cdots \begin{bmatrix}\mathbf{\Delta V^s_{PCC,dq}}\\ \mathbf{\Delta V^{s*}_{PCC,dq}}\end{bmatrix} = \mathbf{Y^{PLL,m}_{\pm,dq}}\begin{bmatrix}\mathbf{\Delta V^s_{PCC,dq}}\\ \mathbf{\Delta V^{s*}_{PCC,dq}}\end{bmatrix} \tag{13}$$

$\mathbf{Y^{PLL,m}_{\pm,dq}}$ is actually the modified sequence-domain admittance model [46]. The four components of the dq-domain admittance model (2) can thus be derived using (9), shown as follows.

$$\begin{aligned}Y^{PLL}_{dd} &= \frac{\mathbf{Y^{CCL}_{cl,dq}} + \mathbf{Y^{CCL*}_{cl,dq}}}{2}\\ Y^{PLL}_{dq} &= j(\frac{\mathbf{Y^{CCL}_{cl,dq}} - \mathbf{Y^{CCL*}_{cl,dq}}}{2} - \mathbf{Y^{PLL}_{cl,dq}} + \mathbf{Y^{PLL*}_{cl,dq}})\\ Y^{PLL}_{qd} &= j(\frac{\mathbf{Y^{CCL*}_{cl,dq}} - \mathbf{Y^{CCL}_{cl,dq}}}{2})\\ Y^{PLL}_{qq} &= \frac{\mathbf{Y^{CCL}_{cl,dq}} + \mathbf{Y^{CCL*}_{cl,dq}}}{2} - \mathbf{Y^{PLL}_{cl,dq}} - \mathbf{Y^{PLL*}_{cl,dq}}\end{aligned} \tag{14}$$

It can be seen from (2) and (14) that the effects of current control loop and PLL on the four components of the dq admittance model can be clearly observed with the help of complex transfer functions. Specifically, PLL dynamics only affect Y^{PLL}_{dq} and Y^{PLL}_{qq}. By substituting (12), (37) and (40) into (14), it can be found that Y^{PLL}_{qq} and Y^{PLL}_{dq} are affected by active power injection $I^s_{g,d}$ and reactive power injection $I^s_{g,q}$, respectively. In addition, the four components of the dq

This article has been accepted for publication in a future issue of this journal, but has not been fully edited. Content may change prior to final publication. Citation information: DOI 10.1109/TEC.2020.2965017, IEEE Transactions on Energy Conversion

impedance model are shown in (15) (L-type filter L_f is used here for simplicity.).

$$\begin{aligned}
Z_{dd}^{PLL} &= Z_{inv} + j\frac{1}{2}\omega_1 L_f (V_{c,q}^s + I_{g,q}^s G_{ci}) G_{PLL} G_{del} V_{dc} / ... \\
&\quad (1 - \frac{1}{2}(V_{c,d}^s + I_{g,d}^s G_{ci}) G_{PLL} G_{del} V_{dc}) \\
Z_{dq}^{PLL} &= -\omega_1 L_f + j\frac{1}{2}(V_{c,q}^s + I_{g,q}^s G_{ci})(L_f s + \frac{1}{2} G_{ci} G_{del} V_{dc}) ... \\
&\quad G_{PLL} G_{del} V_{dc} / (1 - \frac{1}{2}(V_{c,d}^s + I_{g,d}^s G_{ci}) G_{PLL} G_{del} V_{dc}) \\
Z_{qd}^{PLL} &= (\omega_1 L_f) / (1 - \frac{1}{2}(V_{c,d}^s + I_{g,d}^s G_{ci}) G_{PLL} G_{del} V_{dc}) \\
Z_{qq}^{PLL} &= Z_{inv} / (1 - \frac{1}{2}(V_{c,d}^s + I_{g,d}^s G_{ci}) G_{PLL} G_{del} V_{dc})
\end{aligned} \tag{15}$$

where $Z_{inv} = L_f s + \frac{1}{2} V_{dc} G_{ci} G_{del}$. It can be seen from (15) that reactive current injection $I_{g,q}^s$ affects both Z_{dd}^{PLL} and Z_{dq}^{PLL}. Note that the case study in [7] shows that only Z_{dq}^{PLL} is affected by $I_{g,q}^s$, which may be not accurate based on the aforementioned analysis.

2) With Outer Power Control Loop: Similar with (11), the closed-loop response of $\mathbf{\Delta I^s_{g,dq}}$ when further considering power control loop can be derived from Fig. 8, shown as follows.

$$\begin{aligned}
&-\mathbf{\Delta I^s_{g,dq}}\big|_{\mathbf{\Delta P^{ref}_{PQ}}=0} = \mathbf{Y^{CCL1}_{cl,dq}} \mathbf{\Delta V^s_{PCC,dq}} - \mathbf{Y^{PLL1}_{cl,dq}} ... \\
&\mathbf{\Delta V^s_{PCC,dq}} + \mathbf{Y^{PLL1}_{cl,dq}} \mathbf{\Delta V^{s*}_{PCC,dq}} - \mathbf{Y^{PCL1}_{cl,dq}} \mathbf{\Delta V^s_{PCC,dq}} ... \\
&-\mathbf{Y^{PCL2}_{cl,dq}} \mathbf{\Delta V^{s*}_{PCC,dq}}
\end{aligned} \tag{16}$$

where $\mathbf{Y^{CCL1}_{cl,dq}}$ and $\mathbf{Y^{PLL1}_{cl,dq}}$ are the complex transfer function representations of current control loop-related and PLL-related output admittance when considering power control loop, respectively. In addition, $\mathbf{Y^{PCL1}_{cl,dq}}$ and $\mathbf{Y^{PCL2}_{cl,dq}}$ are the power control loop-related output admittance. The detailed expressions are shown as follows.

$$\begin{aligned}
\mathbf{Y^{CCL1}_{cl,dq}} &= \frac{1 + \mathbf{T_{cl,dq}}}{1 + \mathbf{T^{PCL}_{cl,dq}}} \mathbf{Y^{CCL}_{cl,dq}} \\
\mathbf{Y^{PLL1}_{cl,dq}} &= \frac{1 + \mathbf{T_{cl,dq}}}{1 + \mathbf{T^{PCL}_{cl,dq}}} \mathbf{Y^{PLL}_{cl,dq}} \\
\mathbf{Y^{PCL1}_{cl,dq}} &= \frac{2\mathbf{T_{cl,dq}}}{1 + \mathbf{T^{PCL}_{cl,dq}}} \mathbf{G_{+,PLL_i}} \mathbf{V^{s*}_{PCC,dq}} \mathbf{G_{cPQ}} \\
\mathbf{Y^{PCL2}_{cl,dq}} &= \frac{\mathbf{T_{cl,dq}}}{1 + \mathbf{T^{PCL}_{cl,dq}}} (\mathbf{I^s_{g,dq}} - 2\mathbf{G_{+,PLL_i}} \mathbf{V^{s*}_{PCC,dq}}) \mathbf{G_{cPQ}}
\end{aligned} \tag{17}$$

where $\mathbf{T^{PCL}_{cl,dq}} = (1 + \mathbf{G_{cPQ}} \mathbf{V^{s*}_{PCC,dq}}) \mathbf{T_{cl,dq}}$.

Similar with (13), the complex transfer function representation of the dq admittance model when further considering power control loop can be derived based on (16), shown as follows.

$$\mathbf{Y^{PCL,m}_{\pm,dq}} = \begin{bmatrix} \mathbf{Y^{PCL}_{\pm,dd}} & \mathbf{Y^{PCL}_{\pm,dq}} \\ \mathbf{Y^{PCL*}_{\pm,dq}} & \mathbf{Y^{PCL*}_{\pm,dd}} \end{bmatrix} \tag{18}$$

where

$$\begin{aligned}
\mathbf{Y^{PCL}_{\pm,dd}} &= \mathbf{Y^{CCL1}_{cl,dq}} - \mathbf{Y^{PLL1}_{cl,dq}} - \mathbf{Y^{PCL1}_{cl,dq}} \\
\mathbf{Y^{PCL}_{\pm,dq}} &= \mathbf{Y^{PLL1}_{cl,dq}} - \mathbf{Y^{PCL2}_{cl,dq}}
\end{aligned} \tag{19}$$

By substituting (14) and (17) into (19), and applying the inverse transformation of (9), the dq admittance model considering power control loop is shown as follows.

$$\begin{aligned}
Y_{dd}^{PCL} &= \frac{1 + \mathbf{T_{cl,dq}}}{1 + \mathbf{T^{PCL}_{cl,dq}}} Y_{dd}^{PLL} - \frac{\mathbf{T_{cl,dq}} \mathbf{G_{cPQ}}}{1 + \mathbf{T^{PCL}_{cl,dq}}} \frac{P^{ref}}{V_{PCC,d}^s} \\
Y_{dq}^{PCL} &= \frac{1 + \mathbf{T_{cl,dq}}}{1 + \mathbf{T^{PCL}_{cl,dq}}} Y_{dq}^{PLL} + \frac{\mathbf{T_{cl,dq}} \mathbf{G_{cPQ}}}{1 + \mathbf{T^{PCL}_{cl,dq}}} \frac{Q^{ref}}{V_{PCC,d}^s} ... \\
&\quad (2G_{PLL} V_{PCC,d}^s - 1) \\
Y_{qd}^{PCL} &= \frac{1 + \mathbf{T_{cl,dq}}}{1 + \mathbf{T^{PCL}_{cl,dq}}} Y_{qd}^{PLL} - \frac{\mathbf{T_{cl,dq}} \mathbf{G_{cPQ}}}{1 + \mathbf{T^{PCL}_{cl,dq}}} \frac{Q^{ref}}{V_{PCC,d}^s} \\
Y_{qq}^{PCL} &= \frac{1 + \mathbf{T_{cl,dq}}}{1 + \mathbf{T^{PCL}_{cl,dq}}} Y_{qq}^{PLL} + \frac{\mathbf{T_{cl,dq}} \mathbf{G_{cPQ}}}{1 + \mathbf{T^{PCL}_{cl,dq}}} \frac{P^{ref}}{V_{PCC,d}^s} ... \\
&\quad (1 - 2G_{PLL} V_{PCC,d}^s)
\end{aligned} \tag{20}$$

It can be seen from (14) and (20) that, under power control mode, Y_{dd}^{PCL} and Y_{qq}^{PCL} are affected by active power injection P^{ref}. In addition, Y_{dq}^{PCL} and Y_{qd}^{PCL} are affected by reactive power injection Q^{ref}.

Similar with (15), the four components of the dq impedance model (3) can be derived as follows.

$$\begin{aligned}
Z_{dd}^{PCL} &= \frac{BD + CE}{A} \\
Z_{dq}^{PCL} &= \frac{BE - CD}{A} \\
Z_{qd}^{PCL} &= \frac{G_{cPQ} G_{ci} G_{del} I_{g,q}^{ref} B - CF}{A} \\
Z_{qq}^{PCL} &= -\frac{G_{cPQ} G_{ci} G_{del} I_{g,q}^{ref} C + BF}{A}
\end{aligned} \tag{21}$$

where the detailed expressions of $A, B..., F$ are shown in Appendix B. It can be seen from (21) and (43) that, when further considering power control loop, all of the four elements of the dq impedance model are affected by both active and reactive power injection P^{ref} and Q^{ref}.

B. Impacts of Active and Reactive Power References on Low-Frequency Stability

Since low-frequency stability is mainly determined by Z_{qq}^{PCL}, investigation of impacts of P^{ref} and Q^{ref} on Z_{qq}^{PCL} is focused here [18], [27]–[29]. Z_{qq}^{PCL} is reformulated as follows.

$$Z_{qq}^{PCL} = -\frac{\Gamma_1 + \Gamma_2 P^{ref} + \Gamma_3 Q^{ref}}{A} \tag{22}$$

where Γ_1, Γ_2 and Γ_3 are shown as follows.

$$\begin{aligned}
\Gamma_1 &= L_f s + \frac{G_{del} V_{dc} G_{ci} (1 + G_{cPQ} V_{PCC,d}^s)}{2} = \Gamma_{1_1} s + \Gamma_{1_2} \\
\Gamma_2 &= \frac{G_{ci} G_{cPQ} G_{del} L_f s}{V_{PCC,d}^s} + ... \\
&\quad \frac{G_{ci}^2 G_{cPQ} G_{del}^2 V_{dc} (1 + G_{cPQ} V_{PCC,d}^s)}{2 V_{PCC,d}^s} = \Gamma_{2_1} s + \Gamma_{2_2} \\
\Gamma_3 &= \frac{G_{ci} G_{cPQ} G_{del} \omega_1 L_f}{V_{PCC,d}^s}
\end{aligned} \tag{23}$$

This article has been accepted for publication in a future issue of this journal, but has not been fully edited. Content may change prior to final publication. Citation information: DOI 10.1109/TEC.2020.2965017, IEEE Transactions on Energy Conversion

Then, phase angle of Z_{qq}^{PCL} at specific angular frequency ω_0 can be derived as follows.

$$\angle Z_{qq}^{PCL}\big|_{s=j\omega_0} = -180^o + \arctan\frac{(\Gamma_{1\_1}+\Gamma_{2\_1}P^{ref})\omega_0}{\Gamma_{1\_2}+\Gamma_{2\_2}P^{ref}+\Gamma_3 Q^{ref}} \quad (24)$$

It can be seen from (24) that $\angle Z_{qq}^{PCL}$ may be below -90^o for certain combination of P^{ref} and Q^{ref}, which may lead to instability phenomena under weak grid condition.

C. Requirement of Flow Direction and Power Level of Reactive Power Injection for Stability Enhancement

The parameters in (24) except Q_{ref} are guaranteed to be positive. Therefore, if $Q_{ref} \geq 0$, then $\angle Z_{qq}^{PCL} \in (-180^o, -90^o)$, which means that the passivity of Z_{qq}^{PCL} cannot be guaranteed under positive flow direction of reactive power. In other words, negative flow direction of reactive power is required for passivity enforcement. Therefore,

$$\angle Z_{qq}^{PCL} \in (-90^o, -0^o) \leftrightarrow \Gamma_{1\_2}+\Gamma_{2\_2}P^{ref}-\Gamma_3\left|Q^{ref}\right|<0 \quad (25)$$

Based on (25), for a given P^{ref}, passivity of Z_{qq}^{PCL} can be enforced if Q^{ref} satisfies the following inequation.

$$\left|Q^{ref}\right| > \left|Q_{\min}^{ref}\right| = \frac{\Gamma_{1\_2}+\Gamma_{2\_2}P_{ref}}{\Gamma_3} = \left|Q_{\min 1}^{ref}\right| + \left|Q_{\min 2}^{ref}\right| \quad (26)$$

where $\left|Q_{\min 1}^{ref}\right|$ and $\left|Q_{\min 2}^{ref}\right|$ are independent and dependent on active power injection, respectively.

On the other hand, for a given negative Q^{ref}, passivity of Z_{qq}^{PCL} can be enforced if P^{ref} satisfies the following inequation.

$$P^{ref} < P_{\max}^{ref} = \frac{-\Gamma_{1\_2}+\Gamma_3\left|Q_{ref}\right|}{\Gamma_{2\_2}} = P_{\max 1}^{ref} + P_{\max 2}^{ref} \quad (27)$$

where $P_{\max 1}^{ref}$ and $P_{\max 2}^{ref}$ are independent and dependent on reactive power injection, respectively. When the grid impedance is not purely inductive, e.g., the phase angle of grid impedance is lower than 90^o, the allowed maximum delivered active power not to trigger the low-frequency instability is higher than $P_{\max}^{ref}$, and the required minimum reactive power to mitigate the low-frequency instability is lower than $\left|Q_{\min}^{ref}\right|$.

IV. Simulation Verification of Impacts of Active and Reactive Power on Low-Frequency Stability

In this section, the impacts of power control loop, active and reactive power on low-frequency stability derived in Section III are verified by time-domain simulation results in Matlab/Simulink.

A. Impact of Power Control Loop on Low-Frequency Stability

Fig. 9(a) shows Bode diagrams of measured impedance frequency responses of GCI 1 without power control loop $Z_{LCL\_no\_PCL}^{m,mea}$ when $I_{g,d}^{ref} = 1.5$ kA and $I_{g,q}^{ref} = 0$, and with power control loop $Z_{LCL\_with\_PCL}^{m,mea}$ when $P^{ref} = 1.3$ MW and $Q^{ref} = 0$ obtained by frequency scanning method. Z_{dq} and Z_{qd} are omitted, since instability phenomena can be revealed using diagonal elements Z_{dd} and Z_{qq} [7], [18]. Bode diagram of the theoretically-derived dq impedance model without power control loop $Z_{LCL\_no\_PCL}^{m}$ using (2) is also plotted in Fig. 9(a). It can be seen that $Z_{LCL\_no\_PCL}^{m,mea}$ highly agrees with $Z_{LCL\_no\_PCL}^{m}$, which verifies the correctness of the measured impedance data. In addition, Bode diagram of the dq impedance model of frequency-dependent circuit model with one Π section of a 19 km transmission cable, i.e., SCR=1.90, derived by the method presented in Section II is shown as Z_{Ldq}^{m} in Fig. 9(a). Magnitude of $Z_{LCL\_with\_PCL}^{m,mea}$ interacts with that of Z_{Ldq}^{m} at point A (20 Hz), where phase angle difference is $84-(-98) = 182^o$, which indicates that the system is unstable. On the other hand, magnitude of $Z_{LCL\_no\_PCL}^{m,mea}$ interacts with that of Z_{Ldq}^{m} at point B (22 Hz), where phase angle difference is $74.4-(-91.1) = 165.5^o$, which indicates that the system is stable.

Figs. 9(b), (c) show corresponding simulation results with power control loop before 3 s and without power control loop after 3 s. It can be seen that low-frequency oscillation phenomena occur before 3 s. Frequency spectrum of phase A voltage and current before 3 s is shown in Fig. 9(a). It can be seen that oscillation phenomenon occurs at 26.75 Hz ($50-23.25 = 26.75$ Hz) and 73.25 Hz ($50+23.25 = 73.25$ Hz), which verifies correctness of the impedance-based stability analysis. Therefore, the presence of power control loop increases the possibility of instability phenomena in low-frequency range, which agrees with the theoretical analysis results in Section III.A.

B. Impact of Active Power on Low-Frequency Stability

Fig. 10(a) shows Bode diagrams of Z_{dd} and Z_{qq} of dq impedance matrices of GCI 1 as P^{ref} increases from 0.1 MW to 2.0 MW and $Q^{ref} = 0$. It can be seen that magnitude of Z_{qq} decreases in low-frequency range as P^{ref} increases, making magnitude interaction point move leftward and phase angle difference increase. For example, if P^{ref} is increased from 0.5 MW to 2.0 MW, magnitude interaction point of Z_{qq} moves from point C to point D, where phase angle difference is increased from $74-(-95) = 169^o$ to $84-(-98) = 182^o$. It indicates that the system is stable when $P^{ref} = 0.5$ MW, and unstable when $P^{ref} = 2.0$ MW. Similarly, it can be seen that the system is stable when $P^{ref} = 0.1$ MW and unstable when $P^{ref} = 1.3$ MW.

Figs. 10(b), (c) show corresponding simulation results of GCI 1 when P^{ref} changes from 1.3 MW to 0.5 MW at 3 s and from 0.5 MW to 2.0 MW at 6 s. It can be seen that GCI 1 is stable when P^{ref} is 0.5 MW, and is unstable when P^{ref} are 1.3 MW and 2.0 MW, respectively. The simulation results agree with the theoretical analysis result in Fig. 10(a). In addition, frequency spectrum of three-phase voltages and currents from 6 s to 9 s is also shown in Fig. 10(a). It can be seen from Figs. 9(a) and 10(a) that total harmonic distortion (THD) of three-phase voltages increases from 319.92% to 401.98%, and THD of three-phase currents increases from 100.77% to 131.84% once P^{ref} is increased from 1.3 MW to 2.0 MW. In conclusion, higher P^{ref} tends to cause low-frequency instability when the GCI is connected into weak

This article has been accepted for publication in a future issue of this journal, but has not been fully edited. Content may change prior to final publication. Citation information: DOI 10.1109/TEC.2020.2965017, IEEE Transactions on Energy Conversion

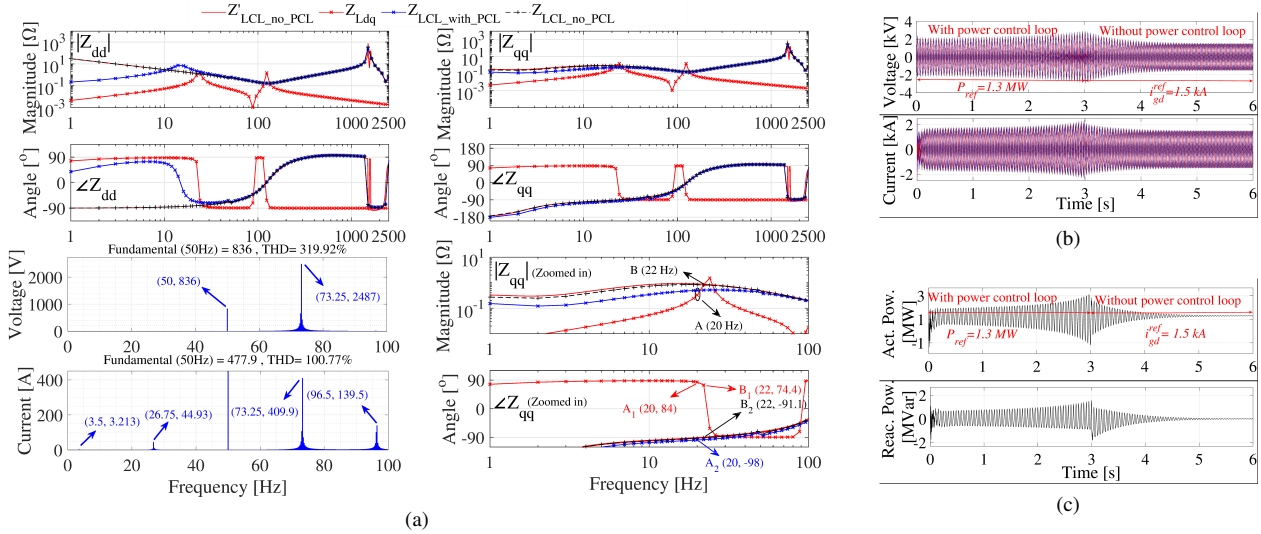

Fig. 9. Impedance-based stability analysis of GCI 1 connected with 19 km transmission cable and simulation results considering effect of power control loop. (a) Bode diagrams. (b) Three-phase voltages and currents. (c) Active and reactive power.

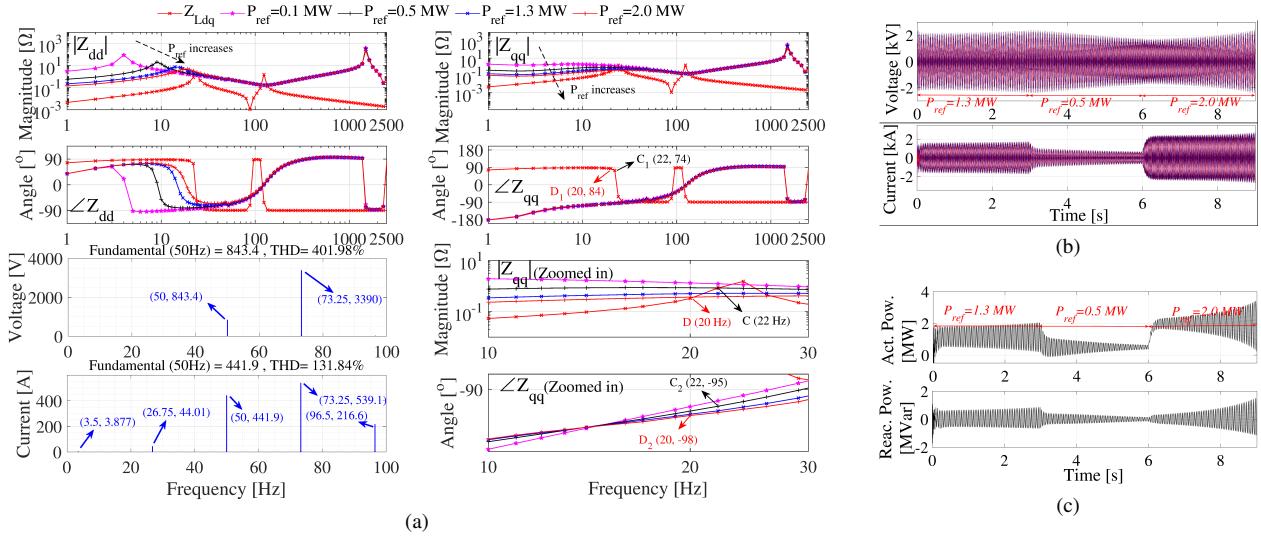

Fig. 10. Impedance-based stability analysis of GCI 1 connected with 19 km transmission cable and simulation results considering effect of different P^{ref} with $Q^{ref} = 0$. (a) Bode diagrams. (b) Three-phase voltages and currents. (c) Active and reactive power.

grid, and brings severer distortion of three-phase voltages and currents, which agrees with the theoretical analysis results in Section III.C.

C. Impact of Reactive Power on Low-Frequency Stability

Fig. 11(a) shows Bode diagrams of output impedances of GCI 1 with $P^{ref} = 2.0$ MW and Q^{ref} changing from 0 MVar to -1.2 MVar. When Q^{ref} is 0 MVar or -0.1 MVar, phase angle difference at magnitude interaction point E of Z_{qq} is $84 - (-99) = 183^o$ or $84 - (-98) = 182^o$, which indicates that the system is unstable. When Q^{ref} is changed to -0.8 MVar and -1.2 MVar, phase angles of Z_{qq} of GCI 1 impedance matrix at magnitude interaction points E and F are within -90^o, which indicates that the system is stable.

Figs. 11(b), (c) show corresponding simulation results of GCI 1 with $P^{ref} = 2.0$ MW and Q^{ref} changing from 0 MVar to -0.8 MVar at 1 s and from -0.8 MVar to -0.1 MVar at 4 s. It can be seen that the system is unstable from 0 s to 1 s, stable from 1 s to 4 s and unstable again from 4 s to 8 s, which agree with the Bode diagrams in Fig. 11(a). It can be seen that negative reactive power of GCI 1 can be adjusted to stabilize the low-frequency oscillation, which agrees with the theoretical analysis results in Section III.C.

V. Impacts of Different Factors on Required Reactive Power for Low-Frequency Stabilization

In this section, impacts of different factors, e.g., PLL parameters, length of transmission cable and number of paralleled GCIs, on required reactive power for low-frequency stabilization are investigated. Real-time verification based on OPAL-RT digital simulator platform is also performed. In addition, comparisons among the presented low-frequency stabilization method and existing commonly-used methods are also performed.

This article has been accepted for publication in a future issue of this journal, but has not been fully edited. Content may change prior to final publication. Citation information: DOI 10.1109/TEC.2020.2965017, IEEE Transactions on Energy Conversion

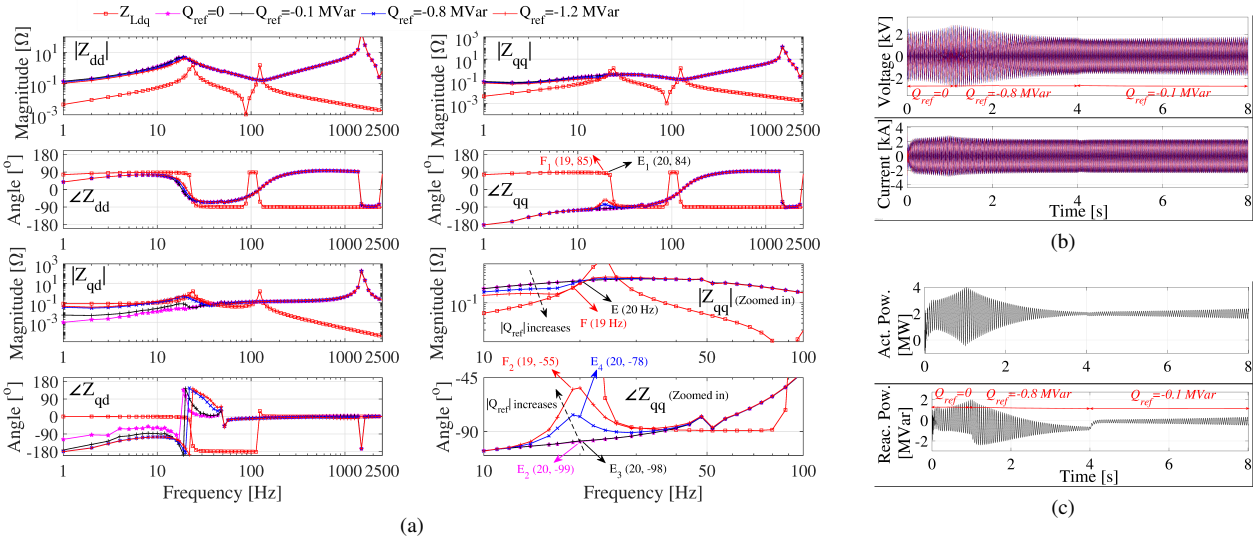

Fig. 11. Impedance-based stability analysis of GCI 1 connected with 19 km transmission cable and simulation results considering effect of different Q^{ref} with $P^{ref} = 2.0$ MW. (a) Bode diagrams. (b) Three-phase voltages and currents. (c) Active and reactive power.

A. Impact of PLL Parameters on Required Reactive Power for Low-Frequency Stabilization

Fig. 12(a) shows Bode diagrams of output impedances of GCI 1 with different PLL controller parameters and Q^{ref}. It can be seen that, when PLL bandwidth $f_{pll} = 56$ Hz ($k_{ppll} = 10$ and $k_{ipll} = 50$) and $Q^{ref} = -0.1$ MVar, phase angle difference at magnitude interaction point A (20 Hz) is $83.57 - (-96.22) = 179.79^o$, which indicates that the system is stable. In addition, when $f_{pll} = 133$ Hz ($k_{ppll} = 24$ and $k_{ipll} = 288$) and $Q^{ref} = -0.1$ MVar, phase angle difference at magnitude interaction point A (20 Hz) is $83.57 - (-99.05) = 182.62^o$, which indicates that the system is unstable. Furthermore, when $f_{pll} = 133$ Hz and $Q_{ref} = -0.6$ MVar, phase angle difference at magnitude interaction point A (20 Hz) is $83.57 - (-87.57) = 171.14^o$, which indicates that the system is stable. Figs. 12(b), (c) show corresponding simulation results when PLL controller parameters and reactive power reference change from $f_{pll} = 56$ Hz and $Q_{ref} = -0.1$ MVar to $f_{pll} = 133$ Hz and $Q_{ref} = -0.1$ MVar at 3 s, to $f_{pll} = 133$ Hz and $Q_{ref} = -0.6$ MVar at 7 s. It can be seen that the system is stable from 0 s to 3 s, unstable from 3 s to 7 s, stable again from 7 s, respectively. Simulation results agree with the impedance-based stability analysis in Fig. 12(a). It can be seen that the GCI with lower PLL bandwidth can be stabilized by less negative reactive power.

B. Impact of Length of Transmission Cable on Required Reactive Power for Low-Frequency Stabilization

Fig. 13(a) shows Bode diagrams of grid impedance and output impedance of GCI 1 with different Q^{ref} when $P^{ref} = 2.0$ MW and $f_{pll} = 89$ Hz ($k_{ppll} = 16$ and $k_{ipll} = 128$). When $L_{TC} = 19$ km and $Q^{ref} = -0.1$ MVar, phase angle difference at magnitude interaction point A (20 Hz) is $83.57 - (-95.86) = 179.43^o$, which indicates that the system is stable. In addition, when $L_{TC} = 20$ km, i.e., SCR=1.80, and $Q_{ref} = -0.1$ MVar, phase angle difference at magnitude interaction point B (17 Hz) is $82.71 - (-99.17) = 181.88^o$, which indicates that the system is unstable. Furthermore, when $L_{TC} = 20$ km and $Q^{ref} = -0.7$ MVar, phase angle difference at magnitude interaction point C (16 Hz) is $84.59 - (-94.50) = 179.09^o$, which indicates that the system is stable again. Figs. 13(b), (c) show corresponding simulation results with length of transmission cable and reactive power reference changing from $L_{TC} = 19$ km and $Q^{ref} = -0.1$ MVar to $L_{TC} = 20$ km and $Q^{ref} = -0.1$ MVar at 4 s, to $L_{TC} = 20$ km and $Q^{ref} = -0.7$ MVar at 6 s. It can be seen that the system is stable from 0 s to 4 s, unstable from 4 s to 6 s, stable again from 6 s, respectively. Frequency spectrum of three-phase voltages and currents when $L_{TC} = 20$ km and $Q^{ref} = -0.1$ MVar is shown in Fig. 13(a). It can be seen that the simulation results agree with the impedance-based stability analysis results. Therefore, weaker grid tends to make system unstable, which can be stabilized by more negative reactive power injection.

C. Impact of Number of Paralleled GCIs on Required Reactive Power for Low-Frequency Stabilization

Fig. 14(a) shows Bode diagrams of the OWPP in Fig. 1(a) with $P^{ref} = 2.0$ MW, $f_{pll} = 89$ Hz, different number of paralleled GCIs N_{GCI} and different Q^{ref}. When $N_{GCI} = 2$, $Q^{ref} = -0.1$ MVar and $N_{GCI} = 2$, $Q^{ref} = -0.7$ MVar, phase angle differences at magnitude interaction points A (19 Hz) and B (17 Hz) are $84.99 - (-97.81) = 182.8^o$ and $86.45 - (-90.02) = 176.47^o$, respectively, which indicate that the system is unstable and stable in the two cases, respectively. In addition, when $N_{GCI} = 4$, $Q^{ref} = -0.7$ MVar, phase angle difference at magnitude interaction point C (11 Hz) is $87.71 - (-104.80) = 192.51^o$, which indicates that the system is unstable. Finally, when $N_{GCI} = 4$, $Q^{ref} = -2.0$ MVar, the Bode diagrams indicate that the system is stable. The corresponding simulation results are shown in Figs. 14(b),

This article has been accepted for publication in a future issue of this journal, but has not been fully edited. Content may change prior to final publication. Citation information: DOI 10.1109/TEC.2020.2965017, IEEE Transactions on Energy Conversion

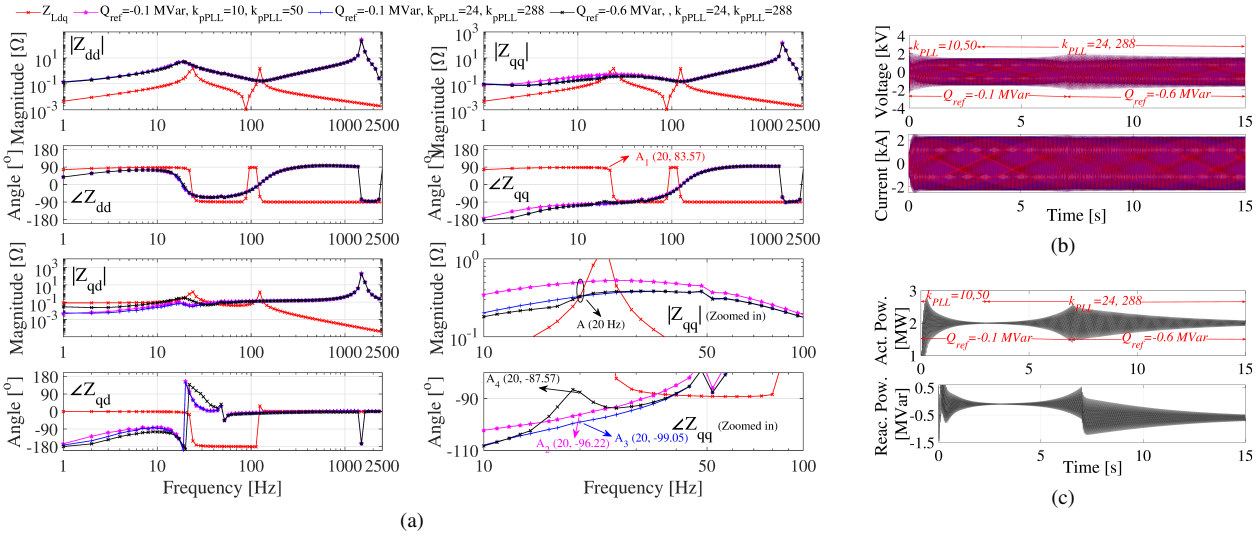

Fig. 12. Impedance-based stability analysis and simulation results of GCI 1 with different PLL controller parameters and Q^{ref}. (a) Bode diagrams. (b) Three-phase voltages and currents. (c) Active and reactive power.

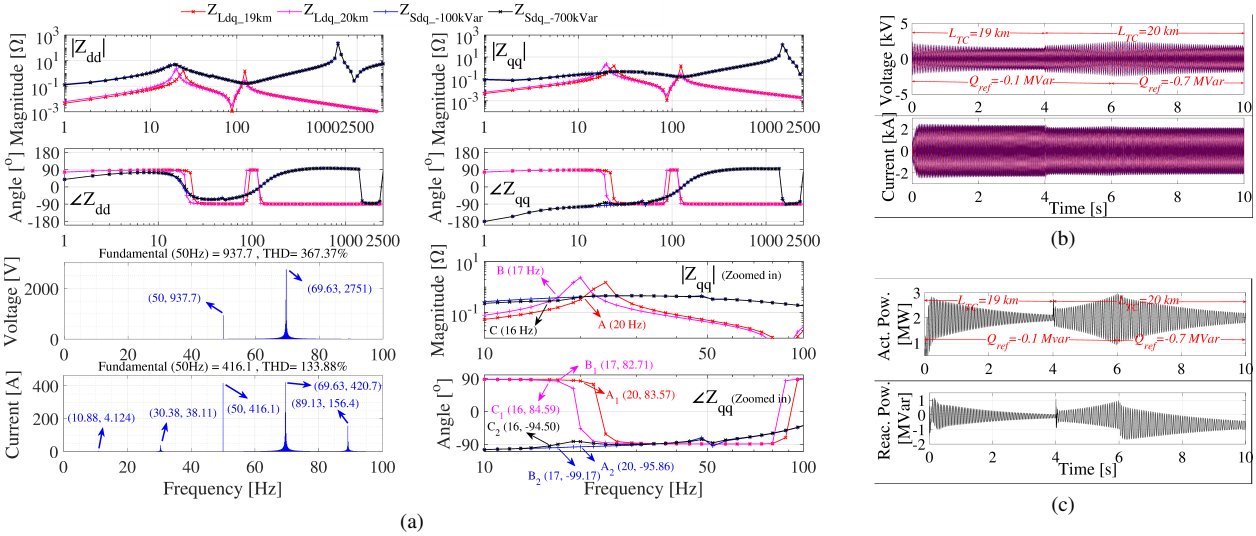

Fig. 13. Impedance-based stability analysis and simulation results of GCI 1 connected with length-scalable transmission cable. (a) Bode diagrams. (b) Three-phase voltages and currents. (c) Active and reactive power.

(c), and collected in the fifth and sixth columns in Table II. In addition, frequency spectrum of three-phase voltages and currents when $N_{GCI} = 2$, $Q^{ref} = -0.7$ MVar is shown in Fig. 14(a). It can be seen that the simulation results agree with the impedance-based stability analysis. In conclusion, integration of more GCIs tends to make OWPP unstable, which can be stabilized by injecting more negative reactive power.

TABLE II
IMPACT OF NUMBER OF PARALLELED GCIS ON REQUIRED REACTIVE POWER FOR LOW-FREQUENCY STABILIZATION

Case	N_{GCI}	Q^{ref}	IBSC	Period	Simulation
Case 1	1	-0.1 MVar	Stable	[0 s, 3.0 s)	Stable
Case 2	2	-0.1 MVar	Unstable	[3.0 s, 4.0 s)	Unstable
Case 3	2	-0.7 MVar	Stable	[4.0 s, 7.0 s)	Stable
Case 4	4	-0.7 MVar	Unstable	[7.0 s, 7.1 s)	Unstable
Case 5	4	-2.0 MVar	Stable	[7.1 s, 10.0 s)	Stable

D. Real-Time Simulation Verification Based on OPAL-RT Platform

Real-time simulation verification based on OPAL-RT digital simulator platform is performed to further validate the correctness of the theoretical analysis results in Section III and the time-domain simulation results obtained by Matlab/Simulink. Fig. 15 shows the picture of the adopted OP5600 real-time digital simulator. The OP5600 combines the power and reliability of Intel Xeon E5 processing cores with the high-performance latest generation Xilinx Virtex-6 FPGA to address a wide range of rapid control prototyping applications with OPAL-RT′s RT-LAB or HYPERSIM software platforms. The Simulink-based model is established in the RT-LAB software, based on which code is generated and downloaded into the OP5600 hardware. Both software and hardware platforms allow high-speed and real-time simulation. The real-time simulation results obtained by OPAL-RT platform are then

This article has been accepted for publication in a future issue of this journal, but has not been fully edited. Content may change prior to final publication. Citation information: DOI 10.1109/TEC.2020.2965017, IEEE Transactions on Energy Conversion

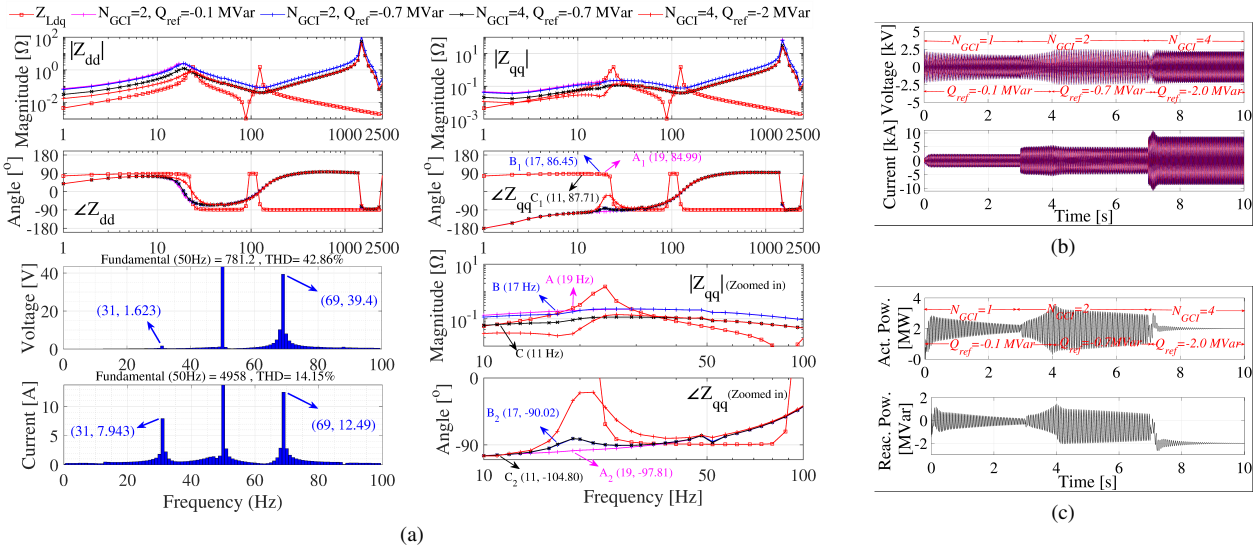

Fig. 14. Impedance-based stability analysis and simulation results of the OWPP shown in Fig. 1(a). (a) Bode diagrams. (b) Three-phase voltages and currents. (c) Active and reactive power.

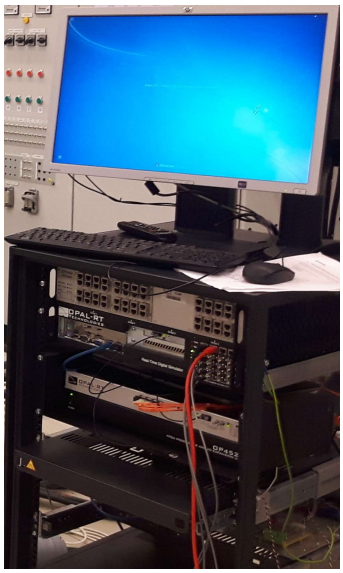

Fig. 15. Picture of the OP5600 real-time digital simulator platform in laboratory.

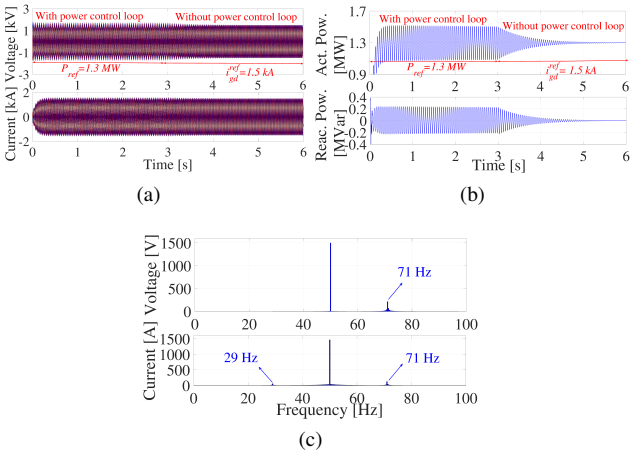

Fig. 16. OPAL-RT platform-based real-time verification of the simulation results in Fig. 9. (a) Three-phase voltages and currents. (b) Active and reactive power. (c) FFT of three-phase voltages and currents with power control loop.

processed in Matlab. The circuit and controller parameters of the GCI used in the real-time simulation verification are shown in Table I.

Fig. 16 shows the real-time verification of the effect of outer power control loop on low-frequency stability. It can be seen that the system is unstable with power control loop before 3 s, and stable without power control loop after 3 s, which agrees with the simulation results based on Matlab/Simulink in Fig. 9.

Fig. 17 shows the real-time verification of the effect of active power delivery on low-frequency stability. It can be seen that the system is unstable with $P_{ref} = 1.3$ MW before 3 s, stable with $P_{ref} = 0.5$ MW between 3 s and 6 s, and unstable again with $P_{ref} = 2.0$ MW after 6 s, which agrees with the simulation results based on Matlab/Simulink in Fig. 10.

Fig. 18 shows the real-time verification of the effect of reactive power injection on low-frequency stability. It can be seen that the system is unstable with $Q_{ref} = 0$ before 1 s, stable with $Q_{ref} = -0.8$ MVar between 1 s and 4 s, and unstable with $Q_{ref} = -0.1$ MVar after 4 s, which agrees with the simulation results based on Matlab/Simulink in Fig. 11.

Fig. 19 shows the real-time verification of the effect of PLL bandwidth on require negative reactive power for low-frequency stabilization. It can be seen that the system is stable with $k_{ppll} = 10$, $k_{ipll} = 50$ and $Q_{ref} = -0.1$ MVar before 3 s, unstable with $k_{ppll} = 24$, $k_{ipll} = 288$ and $Q_{ref} = -0.1$ MVar between 3 s and 7 s, and stable again with $k_{ppll} = 24$, $k_{ipll} = 288$ and $Q_{ref} = -0.6$ MVar after 7 s, which agrees with the simulation results based on Matlab/Simulink in Fig. 12.

This article has been accepted for publication in a future issue of this journal, but has not been fully edited. Content may change prior to final publication. Citation information: DOI 10.1109/TEC.2020.2965017, IEEE Transactions on Energy Conversion

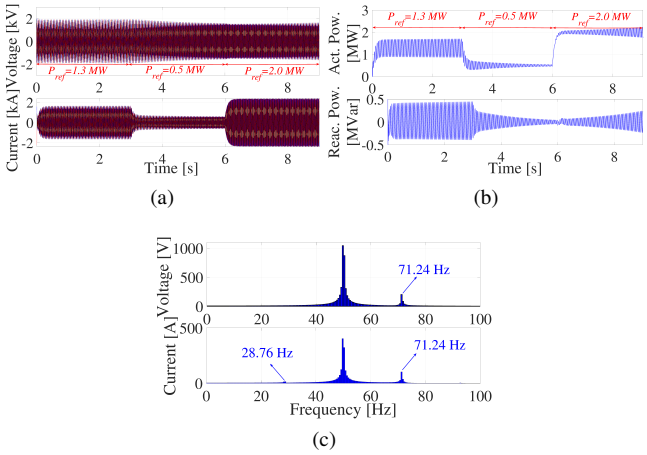

Fig. 17. OPAL-RT platform-based real-time verification of the simulation results in Fig. 10. (a) Three-phase voltages and currents. (b) Active and reactive power. (c) FFT of three-phase voltages and currents between 6 s and 9 s.

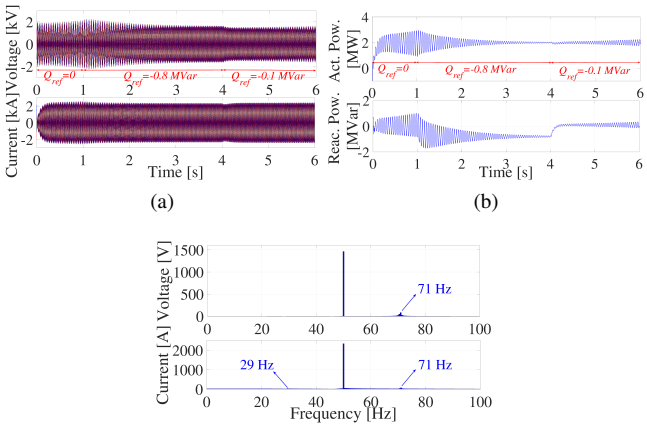

Fig. 18. OPAL-RT platform-based real-time verification of the simulation results in Fig. 11. (a) Three-phase voltages and currents. (b) Active and reactive power. (c) FFT of three-phase voltages and currents between 4 s and 6 s.

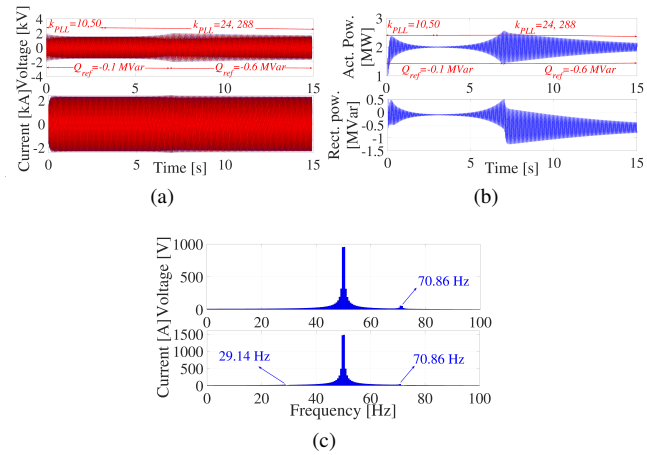

Fig. 19. OPAL-RT platform-based real-time verification of the simulation results in Fig. 12. (a) Three-phase voltages and currents. (b) Active and reactive power. (c) FFT of three-phase voltages and currents between 3 s and 7 s.

E. Discussions of the Presented Low-Frequency Stability Improvement Method Based on Negative Reactive Power Injection

It can be seen from Figs. 11 and 12 that the low-frequency instability phenomenon which occurs when $P^{ref} = 2.0$ MW, $Q^{ref} = -0.1$ MVar, $k_{ppll} = 20$ and $k_{ipll} = 200$ can be mitigated by either increasing negative reactive power injection Q^{ref} from -0.1 MVar to -0.8 MVar or reducing PLL controller parameters from $k_{ppll} = 20$ and $k_{ipll} = 200$ to $k_{ppll} = 10$ and $k_{ipll} = 50$. The low-frequency stabilization method based on PLL controller parameters re-tuning has actually been investigated in [18], [25], [26]. However, phase tracking performance may be weakened, if the PLL bandwidth is decreased. Fig. 20(a) shows the simulation results of q-axis output voltage $V_{PCC,q}$ of PLL when P^{ref} is changed from 2.0 MW to 1.0 MW at 2.0 s with different PLL controller parameters and $Q^{ref} = -0.1$ MVar. It can be seen that the system with lower PLL bandwidth experiences a larger deviation and slower dynamics. Therefore, decreasing PLL bandwidth is actually a trade-off between system stability and PLL dynamics. On the other hand, Fig. 20(b) shows the simulation results of q-axis output voltage $V_{PCC,q}$ of PLL when P^{ref} is changed from 2.0 MW to 1.0 MW at 2.0 s with different amount of negative reactive power injection and $k_{ppll} = 20$, $k_{ipll} = 200$. It can be seen that the system dynamic is slightly affected by reactive power injection, i.e., the presented method is able to improve system low-frequency stability while maintaining fast system dynamics.

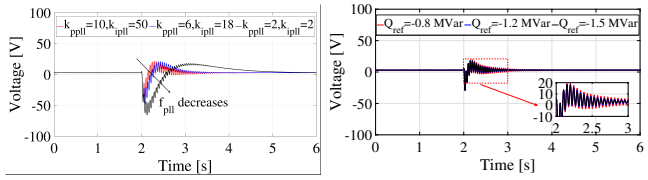

Fig. 20. Simulation results of q-axis output voltage $V_{PCC,q}$ of PLL when P^{ref} is changed from 2.0 MW to 1.0 MW at 2.0 s based on two low-frequency stabilization schemes. (a) Scheme 1: By decreasing PLL controller parameters from $k_{pll} = 20, 200$ to $k_{pll} = 10, 50$, $k_{pll} = 6, 18$ and $k_{pll} = 2, 2$ with $Q^{ref} = -0.1$ MVar. (b) Scheme 2: By increasing negative reactive power injection from $Q^{ref} = -0.1$ MVar to $Q^{ref} = -0.8$ MVar, $Q^{ref} = -1.2$MVar and $Q^{ref} = -1.5$ MVar with $k_{pll} = 20, 200$.

In addition, the low-frequency instability phenomena can also be mitigated based on grid voltage feed-forward control which is able to reshape the output impedance of the GCI [27]–[30]. High proportional feed-forward coefficient G_{ffv} increases $|Z_{qq}|$, which tends to increase stability margin. However, high G_{ffv} also decreases $\angle Z_{qq}$, which tends to decrease stability margin. To further illustrate the two opposite impacts of the usage of grid voltage feed-forward control loop on the low-frequency stability, Figs. 21(a) and (b) show the Bode diagrams of Z_{qq} with different G_{ffv}. It can be seen that when G_{ffv} is 8.6957e-5 or 1.4783e-3, phase angle difference at magnitude interaction points A (20 Hz) and B (21 Hz) are $83.56-(-98.56) = 182.12^o$ or $78.98-(-101.11) = 180.09^o$, respectively, which indicates that the system is unstable under the two cases. In addition, when G_{ffv} is 1.0435e-3 or 1.3043e-

This article has been accepted for publication in a future issue of this journal, but has not been fully edited. Content may change prior to final publication. Citation information: DOI 10.1109/TEC.2020.2965017, IEEE Transactions on Energy Conversion

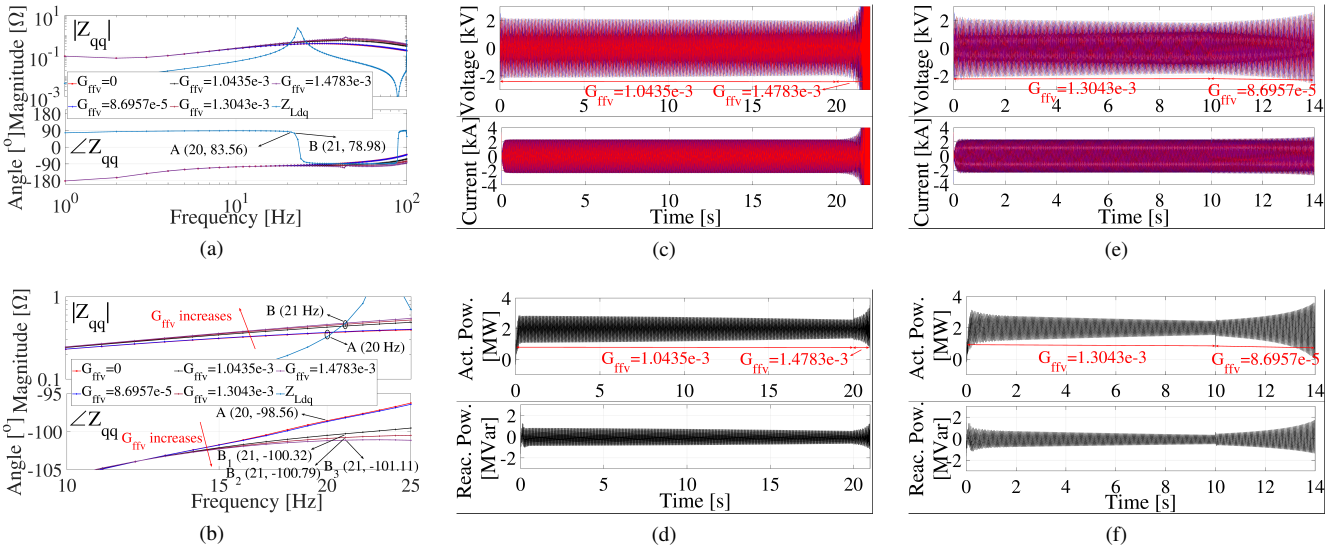

Fig. 21. Impedance-based stability analysis of GCI 1 connected with 19 km transmission cable and simulation results considering effect of different grid voltage feed-forward coefficient G_{ffv}. (a) Bode diagrams of q-q component of dq impedance model. (b) Zoomed Bode diagrams of (a). (c) Three-phase voltages and currents when G_{ffv} is increased from 1.0435e-3 to 1.4783e-3 at 20 s. (d) Active and reactive power when G_{ffv} is increased from 1.0435e-3 to 1.4783e-3 at 20 s. (e) Three-phase voltages and currents when G_{ffv} is decreased from 1.3043e-3 to 8.6957e-5 at 10 s. (d) Active and reactive power when G_{ffv} is decreased from 1.3043e-3 to 8.6957e-5 at 10 s.

3, phase angle difference at magnitude interaction point B (21 Hz) is $78.98-(-100.32)=179.30^o$ or $78.98-(-100.79)=179.77^o$, respectively, which indicates that the system is stable under the two cases. Figs. 21 (c) and (d) show the simulation results when G_{ffv} is increased from 1.0435e-3 to 1.4783e-3 at 20 s, which indicates that the stable system becomes unstable again if larger G_{ffv} is selected. In addition, Figs. 21(e) and (f) show the simulation results when G_{ffv} is decreased from 1.3043e-3 to 8.6957e-5 at 10 s, which indicates that the system becomes unstable again if smaller G_{ffv} is selected. The simulation results in Figs. 21 (c)-(f) agree with the impedance-based stability analysis in Figs. 21 (a) and (b). Both the impedance-based stability analysis and the simulation results indicate that the system can be unstable if too large or too small G_{ffv} is adopted. On the other hand, as derived in Section III.C, the system can be stabilized only if amount of the negative reactive power injection $\left|Q^{ref}\right|$ is larger than $\left|Q^{ref}_{\min}\right|$ which is calculated based on (26).

VI. Conclusion

This paper investigates the impacts of power control loop and reactive power injection on dq impedance model and low-frequency stability of OWPPs, and presents a low-frequency stability improvement strategy based on reshaping the quadrature-axis impedance through injecting negative reactive power. The circuit model of transmission cable considering frequency-dependent characteristics is also established for dq-domain IBSC. Simulation results show that the established circuit model is able to obtain accurate impedance-based stability analysis results. In addition, dq impedance model of GCI is established using transfer matrices and reformulated using complex transfer functions to investigate the effects of different control loops on dq impedance feature, based on which this paper shows that reactive power injection under power control mode is able to affect the quadrature-axis impedance, whereas the quadrature-axis impedance remains unchanged under current control mode. Theoretical analysis also indicates that negative reactive power injection tends to mitigate the low-frequency instability. Specifically, the amount of the required negative reactive power is highly related with length of transmission cable, PLL bandwidth and number of paralleled GCIs. The presented low-frequency stabilization method based on negative reactive power injection is superior to the PLL bandwidth retuning-based method in terms of system dynamic performances, and is superior to the grid voltage feed-forward control-based method in terms of simple structure and robustness. In addition, the maximum bandwidth of the PLL not to violate the low-frequency stability under weak grid condition can be extended with the help of negative reactive power injection. A four PMSGs-based OWPP has been developed in Matlab/Simulink and OPAL-RT real-time digital simulator platform to demonstrate the correctness of the theoretical analysis results.

Appendix A
Complex Transfer Functions Representations of Transfer Matrices in (2) and (3)

A three-phase symmetrical and balanced electrical parameter x_{abc} can be represented in dq reference frame in form of either real space vector x_{dq} (italic letter) or complex space vector $\mathbf{x_{dq}}$ (bold letter), shown as follows [47].

$$x_{dq}=[x_d,x_q]^T \leftrightarrow \mathbf{x_{dq}}=x_d+jx_q \tag{28}$$

In addition, a two-dimensional matrix y^m_{dq} can be repre-

This article has been accepted for publication in a future issue of this journal, but has not been fully edited. Content may change prior to final publication. Citation information: DOI 10.1109/TEC.2020.2965017, IEEE Transactions on Energy Conversion

sented by two complex transfer functions, shown as follows.

$$\begin{aligned} y_{dq}^{m} &= \begin{bmatrix} y_{dd} & y_{dq} \\ y_{qd} & y_{qq} \end{bmatrix} \leftrightarrow \\ \mathbf{y_{+,dq}} &= \frac{y_{dd}+y_{qq}}{2} + j\frac{y_{qd}-y_{dq}}{2} \\ \mathbf{y_{-,dq}} &= \frac{y_{dd}-y_{qq}}{2} + j\frac{y_{qd}+y_{dq}}{2} \end{aligned} \tag{29}$$

where the superscript m indicates that the parameter is a matrix. Based on (28) and (29), the equation using real space vectors and transfer matrices can be reformulated using complex space vectors and complex transfer functions, shown as follows.

$$\begin{aligned} z_{dq} &= y_{dq}^{m} x_{dq} \leftrightarrow \\ \mathbf{z_{dq}} &= \mathbf{y_{+,dq}} \mathbf{x_{dq}} + \mathbf{y_{-,dq}} \mathbf{x_{dq}^{*}} \end{aligned} \tag{30}$$

where $z_{dq} = [z_d, z_q]^T$ and $\mathbf{z_{dq}} = z_d + jz_q$. $\mathbf{x_{dq}^{*}} = x_d - jx_q$ is the complex conjugate of $\mathbf{x_{dq}}$. Specifically, if y_{dq}^{m} is symmetrical, i.e., $y_{dd} = y_{qq} = y_d$ and $y_{qd} = -y_{dq} = y_q$, (30) can be simplified as follows.

$$\mathbf{z_{dq}} = \mathbf{y_{dq}} \mathbf{x_{dq}} \tag{31}$$

where $\mathbf{y_{dq}} = y_d + jy_q$.

According to (29), the transfer matrices in (2) and (3) can be represented as complex transfer functions, shown as follows.

$$Z_{L_{fi}}^{m} = \begin{bmatrix} sL_{fi} & -\omega_1 L_{fi} \\ \omega_1 L_{fi} & sL_{fi} \end{bmatrix} \rightarrow \mathbf{Z_{Lfi}} = sL_{fi} + j\omega_1 L_{fi} \tag{32}$$

where $\omega_1 = 2\pi f_1$ is the fundamental angular frequency and $i = 1, 2$.

$$Z_{C_f}^{m} = \frac{1}{(s^2+\omega_1^2)C_f} \begin{bmatrix} s & \omega_1 \\ -\omega_1 & s \end{bmatrix} \rightarrow \mathbf{Z_{C_f}} = \frac{1}{(s+j\omega_1)C_f} \tag{33}$$

$$G_{del}^{m} = \begin{bmatrix} e^{-1.5T_s s} & 0 \\ 0 & e^{-1.5T_s s} \end{bmatrix} \rightarrow \mathbf{G_{del}} = e^{-1.5T_s s} \tag{34}$$

where T_s is the sampling period.

$$G_{ci}^{m} = \begin{bmatrix} k_{pi} + \frac{k_{ii}}{s} & 0 \\ 0 & k_{pi} + \frac{k_{ii}}{s} \end{bmatrix} \rightarrow \mathbf{G_{ci}} = k_{pi} + \frac{k_{ii}}{s} \tag{35}$$

where k_{pi} and k_{ii} are proportional and integrator coefficients of inner current controller, respectively.

$$\begin{aligned} G_{cPQ}^{m} &= \begin{bmatrix} k_{pPQ} + \frac{k_{iPQ}}{s} & 0 \\ 0 & k_{pPQ} + \frac{k_{iPQ}}{s} \end{bmatrix} \rightarrow \\ \mathbf{G_{cPQ}} &= k_{pPQ} + \frac{k_{iPQ}}{s} \end{aligned} \tag{36}$$

where k_{pPQ} and k_{iPQ} are proportional and integrator coefficients of outer power controller, respectively.

$G_{PLL\_i}^{m}$ models the small-signal perturbation path from PCC voltage in system dq frame to grid current in controller dq frame.

$$\begin{aligned} G_{PLL\_i}^{m} &= \begin{bmatrix} 0 & -I_{g,q}^{s} G_{PLL} \\ 0 & I_{g,d}^{s} G_{PLL} \end{bmatrix} \rightarrow \\ \mathbf{G_{+,PLL\_i}} &= -\mathbf{G_{-,PLL\_i}} = \frac{I_{g,dq}^{s} G_{PLL}}{2} \end{aligned} \tag{37}$$

where $I_{g,d}^{s}$ and $I_{g,q}^{s}$ are d-axis and q-axis components of three-phase currents in system dq frame. In addition, G_{PLL} is defined as follows.

$$G_{PLL} = \frac{k_{ppll} + k_{ipll}/s}{s + V_{PCC,d}^{s}(k_{ppll} + k_{ipll}/s)} \tag{38}$$

where k_{ppll} and k_{ipll} are proportional and integrator coefficients of PLL controller, respectively.

$G_{PLL\_v}^{m}$ models the small-signal perturbation path from PCC voltage in system dq frame to voltage in controller dq frame.

$$\begin{aligned} G_{PLL\_v}^{m} &= \begin{bmatrix} 1 & V_{PCC,q}^{s} G_{PLL} \\ 0 & 1 - V_{PCC,d}^{s} G_{PLL} \end{bmatrix} \rightarrow \\ \mathbf{G_{+,PLL\_v}} &= 1 - \mathbf{V_{PCC,dq}^{s}} G_{PLL}/2 \\ \mathbf{G_{-,PLL\_v}} &= \mathbf{V_{PCC,dq}^{s}} G_{PLL}/2 \end{aligned} \tag{39}$$

where $V_{PCC,d}^{s}$ and $V_{PCC,q}^{s}$ are d-axis and q-axis components of three-phase voltages in system dq frame.

$G_{PLL\_d}^{m}$ models the small-signal perturbation path from PCC voltage in system dq frame to duty cycle in controller dq frame, shown as follows.

$$\begin{aligned} G_{PLL\_d}^{m} &= \begin{bmatrix} 0 & -D_q^{s} G_{PLL} \\ 0 & D_d^{s} G_{PLL} \end{bmatrix} \rightarrow \\ \mathbf{G_{+,PLL\_d}} &= -\mathbf{G_{-,PLL\_d}} = \frac{\mathbf{D_{dq}^{s}} G_{PLL}}{2} \end{aligned} \tag{40}$$

where D_d^{s} and D_q^{s} are d-axis and q-axis components of three-phase duty cycles in system dq frame.

In addition, $G_{PQ\_i}^{m}$ and $G_{PQ\_v}^{m}$ model the small-signal dynamics of power control loop, shown as follows.

$$G_{PQ\_i}^{m} = \begin{bmatrix} V_{PCC,d}^{s} & V_{PCC,q}^{s} \\ -V_{PCC,q}^{s} & V_{PCC,d}^{s} \end{bmatrix} \rightarrow \mathbf{G_{PQ\_i}} = \mathbf{V_{PCC,dq}^{s*}} \tag{41}$$

$$\begin{aligned} G_{PQ\_v}^{m} &= \begin{bmatrix} -I_{g,d}^{s} & -I_{g,q}^{s} \\ -I_{g,q}^{s} & I_{g,d}^{s} \end{bmatrix} \rightarrow \\ \mathbf{G_{+,PQ\_v}} &= 0 \qquad \mathbf{G_{-,PQ\_v}} = -\mathbf{I_{g,dq}^{s}} \end{aligned} \tag{42}$$

This article has been accepted for publication in a future issue of this journal, but has not been fully edited. Content may change prior to final publication. Citation information: DOI 10.1109/TEC.2020.2965017, IEEE Transactions on Energy Conversion

APPENDIX B
DETAILED EXPRESSIONS OF PARAMETERS IN (21)

$$
\begin{aligned}
A &= \frac{G_{cPQ}G_{ci}^2G_{del}^2(G_{cPQ}+G_{PLL})[(P^{ref})^2+(Q^{ref})^2]}{(V_{PCC,d}^s)^2}+\dots\\
&\quad G_{PLL}G_{del}[\frac{0.5V_{dc}G_{ci}P^{ref}+(V_{PCC,d}^s)^2-\omega_1L_fQ^{ref}}{0.5V_{dc}V_{PCC,d}^s}]+\dots\\
&\quad \frac{G_{PLL}G_{cPQ}G_{ci}G_{del}^2P^{ref}}{0.5V_{dc}}-1\\
B &= L_fs+\frac{G_{del}V_{dc}G_{ci}(1+G_{cPQ}V_{PCC,d}^s)}{2}\\
C &= \omega_1L_f\\
D &= \frac{G_{del}G_{PLL}V_{PCC,d}^s}{0.5V_{dc}}+\frac{G_{ci}G_{del}(G_{cPQ}+G_{PLL})P^{ref}}{V_{PCC,d}^s}-\dots\\
&\quad \frac{\omega_1L_fG_{del}G_{PLL}Q^{ref}}{0.5V_{dc}V_{PCC,d}^s}-1\\
E &= \frac{\omega_1L_fG_{del}G_{PLL}P^{ref}}{0.5V_{dc}V_{PCC,d}^s}+\frac{G_{ci}G_{del}(G_{cPQ}+G_{PLL})Q_{ref}}{V_{PCC,d}^s}\\
F &= 1+\frac{G_{ci}G_{cPQ}G_{del}P^{ref}}{V_{PCC,d}^s}
\end{aligned}
\tag{43}
$$

REFERENCES

[1] P. Bresesti, W. L. Kling, R. L. Hendriks, and R. Vailati, "HVDC connection of offshore wind farms to the transmission system," *IEEE Trans, Energy Convers.*, vol. 22, no. 1, pp. 37–43, Mar. 2007.

[2] F. Blaabjerg, Z. Chen, and S. B. Kjaer, "Power electronics as efficient interface in dispersed power generation systems," *IEEE Trans. Power Electron.*, vol. 19, no. 5, pp. 1184–1194, Sep. 2004.

[3] S. Shah and L. Parsa, "Impedance modeling of three-phase voltage source converters in DQ, sequence, and phasor domains," *IEEE Trans. Energy Convers.*, vol. 32, no. 3, pp. 1139–1150, Sep. 2017.

[4] I. Vieto and J. Sun, "Sequence impedance modeling and analysis of type-III wind turbines," *IEEE Trans. Energy Convers.*, vol. 33, no. 2, pp. 537–545, Jun. 2018.

[5] H. Liu, X. Xie, and Z. Liu, "Comparative studies on the impedance models of VSC-based renewable generators for SSI stability analysis," *IEEE Trans. Energy Convers.*, vol. 34, no. 3, pp. 1442–1453, Sep. 2019.

[6] W. Zhou, Y. Wang, and Z. Chen, "Impedance-decoupled modelling method of multi-port transmission network in inverter-fed power plant," *IEEE Trans. Ind. Appl.*, Early Access.

[7] B. Wen, D. Boroyevich, R. Burgos, P. Mattavelli, and Z. Shen, "Analysis of DQ small-signal impedance of grid-tied inverters," *IEEE Trans. Power Electron.*, vol. 31, no. 1, pp. 675–687, Jan. 2016.

[8] Y. Wang, X. Wang, F. Blaabjerg, and Z. Chen, "Harmonic instability assessment using state-space modeling and participation analysis in inverter-fed power systems," *IEEE Trans. Ind. Electron.*, vol. 64, no. 1, pp. 806–816, Jan. 2017.

[9] J. Sun, "Impedance-based stability criterion for grid-connected inverters," *IEEE Trans. Power Electron.*, vol. 26, no. 11, p. 3075, Nov. 2011.

[10] S. Zhang, S. Jiang, X. Lu, B. Ge, and F. Z. Peng, "Resonance issues and damping techniques for grid-connected inverters with long transmission cable," *IEEE Trans. Power Electron.*, vol. 29, no. 1, pp. 110–120, Jan. 2014.

[11] Y. Song, E. Ebrahimzadeh, and F. Blaabjerg, "Analysis of high-frequency resonance in DFIG-based offshore wind farm via long transmission cable," *IEEE Trans. Energy Convers.*, vol. 33, no. 3, pp. 1036–1046, Sep. 2018.

[12] I. Erlich, M. Wilch, and C. Feltes, "Reactive power generation by DFIG based wind farms with AC grid connection," in *Proc. 2007 IEEE European Conference on Power Electronics and Applications*, pp. 1–10.

[13] L. Xu and L. Fan, "Impedance-based resonance analysis in a VSC-HVDC system," *IEEE Trans. Power Del.*, vol. 28, no. 4, pp. 2209–2216, Oct. 2013.

[14] M. Amin, M. Molinas, J. Lyu, and X. Cai, "Impact of power flow direction on the stability of VSC-HVDC seen from the impedance nyquist plot," *IEEE Trans. Power Electron.*, vol. 32, no. 10, pp. 8204–8217, Oct. 2017.

[15] K. M. Alawasa, Y. A.-R. I. Mohamed, and W. Xu, "Active mitigation of subsynchronous interactions between PWM voltage-source converters and power networks," *IEEE Trans. Power Electron.*, vol. 29, no. 1, pp. 121–134, Jan. 2014.

[16] H. Zhao, Q. Wu, J. Wang, Z. Liu, M. Shahidehpour, and Y. Xue, "Combined active and reactive power control of wind farms based on model predictive control," *IEEE Trans. Energy Convers.*, vol. 32, no. 3, pp. 1177–1187, Sep. 2017.

[17] W. Zhou, Y. Wang, D. Liu, and Z. Chen, "Optimization of active and reactive power dispatch among multi-paralleled grid-connected inverters considering low-frequency stability," in *Proc. 2019 IEEE 45th Annual Conference of the IEEE Industrial Electronics Society (IECON)*, pp. 6024–6031.

[18] S. Zhou, X. Zou, D. Zhu, L. Tong, Y. Zhao, Y. Kang, and X. Yuan, "An improved design of current controller for LCL-type grid-connected converter to reduce negative effect of PLL in weak grid," *IEEE J. Emerg. Sel. Topics Power Electron.*, vol. 6, no. 2, pp. 648–663, Jun. 2018.

[19] N. Pogaku, M. Prodanovic, and T. C. Green, "Modeling, analysis and testing of autonomous operation of an inverter-based microgrid," *IEEE Trans. Power Electron.*, vol. 22, no. 2, pp. 613–625, Mar. 2007.

[20] J. Lyu, X. Cai, and M. Molinas, "Frequency domain stability analysis of MMC-based HVDC for wind farm integration," *IEEE J. Emerg. Sel. Topics Power Electron.*, vol. 4, no. 1, pp. 141–151, Mar. 2016.

[21] M. Liserre, R. Teodorescu, and F. Blaabjerg, "Stability of photovoltaic and wind turbine grid-connected inverters for a large set of grid impedance values," *IEEE Trans. Power Electron.*, vol. 21, no. 1, pp. 263–272, Jan. 2006.

[22] Y. Xia, Y. Peng, P. Yang, Y. Li, and W. Wei, "Different influence of grid impedance on low-and high-frequency stability of PV generators," *IEEE Trans. Ind. Electron.*, vol. 66, no. 11, pp. 8498–8508, Nov. 2019.

[23] S. Liu, P. X. Liu, and X. Wang, "Stochastic small-signal stability analysis of grid-connected photovoltaic systems," *IEEE Trans. Ind. Electron.*, vol. 63, no. 2, pp. 1027–1038, Feb. 2016.

[24] W. Wei, Y. Xia, and F. Blaabjerg, "Nonlinear stability analysis for three-phase grid-connected PV generators," *IEEE J. Emerg. Sel. Topics Power Electron.*, Early Access.

[25] M. Cespedes and J. Sun, "Adaptive control of grid-connected inverters based on online grid impedance measurements," *IEEE Trans. Sustain. Energy*, vol. 5, no. 2, pp. 516–523, Apr. 2014.

[26] M. Amin and M. Molinas, "A gray-box method for stability and controller parameter estimation in HVDC-connected wind farms based on nonparametric impedance," *IEEE Trans. Ind. Electron.*, vol. 66, no. 3, pp. 1872–1882, Mar. 2019.

[27] J. Fang, X. Li, H. Li, and Y. Tang, "Stability improvement for three-phase grid-connected converters through impedance reshaping in quadrature-axis," *IEEE Trans. Power Electron.*, vol. 33, no. 10, pp. 8365–8375, Oct. 2017.

[28] X. Zhang, D. Xia, Z. Fu, G. Wang, and D. Xu, "An improved feedforward control method considering PLL dynamics to improve weak grid stability of grid-connected inverters," *IEEE Trans. Ind. Appl.*, vol. 54, no. 5, pp. 5143–5151, Sep./Oct. 2018.

[29] D. Yang, X. Wang, F. Liu, K. Xin, Y. Liu, and F. Blaabjerg, "Symmetrical PLL for SISO impedance modeling and enhanced stability in weak grids," *IEEE Trans. Power Electron.*, 2019, Early Access.

[30] T. Messo, R. Luhtala, A. Aapro, and T. Roinila, "Accurate impedance model of a grid-connected inverter for small-signal stability assessment in high-impedance grids," in *Proc. 2018 IEEE IPEC-ECCE ASIA*, pp. 3156–3163.

[31] Á. Molina-García, R. A. Mastromauro, T. García-Sánchez, S. Pugliese, M. Liserre, and S. Stasi, "Reactive power flow control for PV inverters voltage support in LV distribution networks," *IEEE Trans. Smart Grid*, vol. 8, no. 1, pp. 447–456, Jan. 2017.

[32] D. Yang, X. Wang, F. Liu, K. Xin, Y. Liu, and F. Blaabjerg, "Adaptive reactive power control of PV power plants for improved power transfer capability under ultra-weak grid conditions," *IEEE Trans. Smart Grid*, vol. 10, no. 2, pp. 1269–1279, Mar. 2019.

[33] R. A. Jabr, "Linear decision rules for control of reactive power by distributed photovoltaic generators," *IEEE Trans. Power Syst.*, vol. 33, no. 2, pp. 2165–2174, Mar. 2018.

[34] X. Wang, F. Blaabjerg, and P. C. Loh, "Passivity-based stability analysis and damping injection for multiparalleled VSCs with LCL filters," *IEEE Trans. Power Electron.*, vol. 32, no. 11, pp. 8922–8935, Nov. 2017.

[35] H.-C. Chen, P.-T. Cheng, and X. Wang, "A passivity-based stability analysis of the active damping technique in the offshore wind farm applications," *IEEE Trans. Ind. Appl.*, vol. 54, no. 5, pp. 5074–5082, Sep./Oct. 2018.
[36] W. Zhou, Y. Wang, and Z. Chen, "Frequency and temperature-dependent power cable modelling for small-signal stability analysis of grid-connected inverter system," in *Proc. 2018 IEEE 4th Southern Power Electronics Conference (SPEC)*, pp. 1–8.
[37] J. Beerten, S. D'Arco, and J. A. Suul, "Frequency-dependent cable modelling for small-signal stability analysis of VSC-HVDC systems," *IET Gen., Transm. Distrib.*, vol. 10, no. 6, pp. 1370–1381, May 2016.
[38] ——, "Identification and small-signal analysis of interaction modes in VSC MTDC systems," *IEEE Trans. Power Del.*, vol. 31, no. 2, pp. 888–897, Apr. 2016.
[39] Q. Hao, Z. Li, F. Gao, and J. Zhang, "Reduced-order small-signal models of modular multilevel converter and MMC-based HVdc grid," *IEEE Trans. Ind. Electron.*, vol. 66, no. 3, pp. 2257–2268, Mar. 2019.
[40] S. Golestan, J. M. Guerrero, and J. C. Vasquez, "Three-phase PLLs: A review of recent advances," *IEEE Trans. Power Electron.*, vol. 32, no. 3, pp. 1894–1907, Mar. 2017.
[41] C. R. Paul, *Analysis of multiconductor transmission lines*. John Wiley & Sons, 2008.
[42] W. Zhou, Y. Wang, and Z. Chen, "Vector fitting-based reduced order modelling method for power cables," in *Proc. IET 15th International Conference on AC and DC Power Transmission (ACDC 2019)*, pp. 1–6.
[43] B. Gustavsen and A. Semlyen, "Rational approximation of frequency domain responses by vector fitting," *IEEE Trans. Power Del.*, vol. 14, no. 3, pp. 1052–1061, Jul. 1999.
[44] A. Rygg, M. Molinas, C. Zhang, and X. Cai, "On the equivalence and impact on stability of impedance modeling of power electronic converters in different domains," *IEEE J. Emerg. Sel. Topics Power Electron.*, vol. 5, no. 4, pp. 1444–1454, Dec. 2017.
[45] C. Dufour, H. Saad, J. Mahseredjian, and J. Bélanger, "Custom-coded models in the state space nodal solver of ARTEMiS," in *Proceeding 2013 International Conference on Power System Transients (IPST)*.
[46] X. Wang, L. Harnefors, and F. Blaabjerg, "Unified impedance model of grid-connected voltage-source converters," *IEEE Trans. Power Electron.*, vol. 33, no. 2, pp. 1775–1787, Feb. 2018.
[47] L. Harnefors, "Modeling of three-phase dynamic systems using complex transfer functions and transfer matrices," *IEEE Trans. Ind. Electron.*, vol. 54, no. 4, pp. 2239–2248, Aug. 2007.

Weihua Zhou (S'18) was born in Anhui, China, in 1993. He received the B.Eng. and M.Sc. degrees in electrical engineering from the School of Automation, Northwestern Polytechnical University, Xi'an, China, in 2014 and 2017, respectively. He is currently working toward the Ph.D. degree in electrical engineering with the Department of Energy Technology, Aalborg University, Aalborg, Denmark.

From November 2015 to May 2016, he was a Junior Research Assistant at the Department of Mechanical and Automation Engineering, The Chinese University of Hong Kong, Hong Kong. His research interests include modeling and control of grid-connected converters, and small-signal stability analysis of power electronic-dominated power systems.

Mr. Zhou was the recipient of the Best Paper Award in 6th International Conference on Smart Grids (icSmartGrid) cosponsored by IEEE Industry Application Society in 2018.

Yanbo Wang (S'15-M'17) received the Ph.D. degree in electrical engineering at the Department of Energy Technology, Aalborg University, Aalborg, Denmark, in 2017. Currently, he is with the Department of Energy Technology in Aalborg University as an Assistant Professor.

From June to October of 2016, he was a visiting scholar in Power System Research Group of the Department of Electrical and Computer Engineering, University of Manitoba, Winnipeg, MB, Canada. His research interests include distributed power generation system, wind power system, microgrid, as well as operation and control technologies of power electronic-dominated power system.

Dr. Wang's paper on Distributed Power System received the First Prize Paper Award of the 6th International Conference of Smart Grid cosponsored by IEEE Industry Application Society in 2018. He received the Best Session Paper Award at the annual conference of the IEEE Industrial Electronics Society in 2015 in Japan.

Raymundo E. Torres-Olguin received the B.Sc. degree in electromechanical engineering from the University of San Luis Potosí, Mexico, in 2004, M.Sc. degree in control and dynamical systems from the Applied Mathematics Department, Research Institute of Science and Technology of San Luis Potosí (IPICYT), Mexico, in 2006, and Ph.D. degree in electric power engineering from the Norwegian University of Science and Technology (NTNU), Norway, in 2013.

From 2012, he has worked as a research scientist in SINTEF Energy Research located in Trondheim, Norway. His main research interest includes control of power electronics for the integration of renewable resources, dc transmission, and microgrids.

Zhe Chen (M'95-SM'98-F'19) received the B.Eng. and M.Sc. degrees all in electrical engineering from Northeast China Institute of Electric Power Engineering, Jilin City, China, MPhil in power electronic from Staffordshire University, England and the Ph.D. degree in electrical engineering from University of Durham, England.

Dr. Chen is a full Professor with the Department of Energy Technology, Aalborg University, Aalborg, Denmark. He is the leader of Wind Power System Research program at the Department of Energy Technology, Aalborg University and the Danish Principle Investigator for Wind Energy of Sino-Danish Centre for Education and Research. His research areas are power systems, power electronics and electric machines, and his main current research interests are wind energy and modern power systems. He has led many research projects and has more than 500 publications in his technical fields.